Storm-Scale Data Assimilation and Ensemble Forecasting with the NSSL Experimental Warn-on-Forecast System. Part II: Combined Radar and Satellite Data Experiments

THOMAS A. JONES, KENT KNOPFMEIER, DUSTAN WHEATLEY, AND GERALD CREAGER

Cooperative Institute for Mesoscale Meteorological Studies, University of Oklahoma, Norman, Oklahoma

PATRICK MINNIS

NASA Langley Research Center, Hampton, Virginia

RABINDRA PALIKONDA

Science Systems and Applications, Inc., Hampton, Virginia

(Manuscript received 26 August 2015, in final form 16 December 2015)

ABSTRACT

This research represents the second part of a two-part series describing the development of a prototype ensemble data assimilation system for the Warn-on-Forecast (WoF) project known as the NSSL Experimental WoF System for ensembles (NEWS-e). Part I describes the NEWS-e design and results from radar reflectivity and radial velocity data assimilation for six severe weather events occurring during 2013 and 2014. Part II describes the impact of assimilating satellite liquid and ice water path (LWP and IWP, respectively) retrievals from the GOES Imager along with the radar observations. Assimilating LWP and IWP observations may improve thermodynamic conditions at the surface over the storm-scale domain through better analysis of cloud coverage in the model compared to radar-only experiments. These improvements sometimes corresponded to an improved analysis of supercell storms leading to better forecasts of low-level vorticity. This positive impact was most evident for events where convection is not ongoing at the beginning of the radar and satellite data assimilation period. For more complex cases containing significant amounts of ongoing convection, only assimilating clear-sky satellite retrievals in place of clear-air reflectivity resulted in spurious regions of light precipitation compared to the radar-only experiments. The analyzed tornadic storms in these experiments are sometimes too weak and quickly diminished in intensity in the forecasts. The lessons learned as part of these experiments should lead to improved iterations of the NEWS-e system, building on the modestly successful results described here.

1. Introduction

Assimilating both high-resolution ground-based radar and satellite observations into convection-allowing numerical weather prediction (NWP) models has led to significant advances in the forecasting of storm-scale precipitation and severe weather events during the last decade. In the United States, the Weather Surveillance Radar-1988 Doppler (WSR-88D) network provides a 3D volume of radar reflectivity and Doppler radial velocity over much of the country, though the near-surface (0–2 km) coverage is limited to near the radar sites only (Crum and Alberty 1993). Many studies have analyzed the impacts of assimilating radar data and found that both radial velocity and reflectivity provide information leading to improvements in storm-scale forecasting (e.g., Dowell et al. 2004; Gao et al. 2004; Aksoy et al. 2009, 2010; Dawson et al. 2012; Gao and Stensrud 2012; Yussouf et al. 2013). Assimilating radial velocity was the focus of several early studies (Snyder and Zhang 2003; Zhang et al. 2004) with the assimilation of radar reflectivity becoming an important topic of research in follow-up work (Dowell et al. 2004; Tong and Xue 2005; Aksoy et al. 2009, 2010; Yussouf and Stensrud 2010; Dowell et al. 2011; Yussouf et al. 2013). Radar reflectivity may be assimilated by either relating it to a

Corresponding author address: Dr. Thomas A. Jones, Cooperative Institute for Mesoscale Meteorological Studies, University of Oklahoma, 120 David L. Boren Blvd., Norman, OK 73072.
E-mail: thomas.jones@noaa.gov

DOI: 10.1175/WAF-D-15-0107.1

latent heat tendency (e.g., Hu and Xue 2007) or directly relating reflectivity to the cloud hydrometeor properties of precipitating clouds (e.g., Dowell et al. 2011). The latter requires advanced cloud microphysics that when applied can generate an accurate analysis of convection within the model (Tong and Xue 2005; Yussouf et al. 2013). The goal of many radar data assimilation studies is to create an accurate analysis of mature convection to improve forecasts of severe weather events such as high winds and tornadoes in the 0–1-h time frame. This also represents one of the key goals of the Warn-on-Forecast (WoF) project (Stensrud et al. 2009, 2013), and much work is still needed on this topic. However, capturing the early development of storms and the near-storm environment is equally important to fulfill the WoF goals, but has received somewhat less attention.

One important disadvantage of radar data assimilation is that it does not capture the nonprecipitation phase of cloud development during convective initiation nor does it provide much information from the near-storm environment. Forecasting convection initiation has proven to be challenging (Kain et al. 2013) and determining a way to assimilate information relating to convection initiation is receiving greater interest in the research community (e.g., Mecikalski et al. 2013). As a result, assimilating high-resolution satellite observations has also recently received a high degree of attention (Vukicevic et al. 2004, 2006; Otkin 2010; Polkinghorne et al. 2010; Pincus et al. 2011; Polkinghorne and Vukicevic 2011; Zupanski et al. 2011; Jones et al. 2013b, 2015; Zhang et al. 2013; Kerr et al. 2015). For storm-scale applications, high spatial and temporal frequency observations are required, which are currently available from the imager aboard the operational GOES satellites (Menzel and Purdom 1994). The imager measures upwelling visible and infrared radiation that is sensitive to surface conditions, cloud cover, cloud type, and atmospheric moisture and temperature properties. The observed radiances may be assimilated directly into an NWP model through the use of a radiative transfer model (RTM) or through retrieval algorithms, which derive cloud properties, moisture, and/or temperature profiles from the raw radiances. The former method is generally more computationally intensive and has large uncertainties in cloudy regions (e.g., Zupanski et al. 2011), while the latter is easier to relate to atmospheric variables, but must also accounts for the uncertainties in the retrieval algorithms. However, the overall information content from both methods has been found to be similar (Migliorini 2012). Jones et al. (2013b) assimilated cloud water path (CWP) retrievals (Minnis et al. 2008a,b, 2011) from the *GOES-13* satellite for a severe weather event occurring on 10 May 2010. Results showed that assimilating CWP retrievals at 15-min intervals over a 3-h period generated a better representation of convection and suppressed development of spurious convection within the model compared to an experiment that did not assimilate CWP retrievals.

Assimilating both high-resolution radar and satellite data simultaneously is currently in its infancy. Using observing system simulation experiments (OSSEs) for a winter weather event, Jones et al. (2013a, 2014) show that assimilating radar reflectivity and Doppler radial velocity with simulated GOES-R Advanced Baseline Imager (ABI) water vapor sensitive radiances generally performed better than assimilating each individually for mesoscale experiments. Jones et al. (2015) extended the CWP retrieval research conducted by Jones et al. (2013b) by assimilating CWP using an improved forward operator along with assimilating radar reflectivity and radial velocity using the techniques developed by Zhang et al. (2004) and Dowell et al. (2004). Jones et al. (2015) showed that assimilating CWP observations in conjunction with radar data led to quicker spinup of convection, reduction of spurious cloud cover in actual clear-sky regions, and improved characterization of the anvil features of mature convection. Still, these results were only valid for a single case study. Additional cases are required to determine how general the improvements from assimilating CWP are and what potential disadvantages it may have compared to assimilating radar data alone for various environments.

This research represents the second part in a two-part series describing the development of a convection-allowing analysis and forecasting system that assimilates radar and satellite data to create ensemble forecasts of severe weather events. The first part of this research (Wheatley et al. 2015, hereafter Part I) analyzes the impact of radar data assimilation using the National Severe Storms Laboratory (NSSL) Experimental WoF System for ensembles (NEWS-e) for six events occurring during 2013 and 2014. All six events were associated with severe convection and strong tornadoes (Table 1). The 2013 events that occurred on 19, 20, and 31 May in central Oklahoma consisted of supercells in a high-shear, high-instability environment with little convection present prior to initiation of these storms. The 2014 events are more complex. The 27 and 28 April events are centered over Arkansas and Mississippi, respectively, with generally lower atmospheric instability and significant convection ongoing throughout the morning and early afternoon hours. The final event on 11 May 2014 occurred in Nebraska where convection formed along a stationary front, behind which existed areas of stratiform precipitation and thick cloud cover. The variety of these cases should allow for a

TABLE 1. Summary of each of the tornado-producing events studied. Touchdown times and Enhanced Fujita (EF) scale ratings for the tornado of interest are provided along with the time radar and satellite data assimilation (DA) begins.

Date	Tornado	Touchdown (UTC)	EF scale rating	DA start time (UTC)
19 May 2013	Edmond–Carney, OK	2122; 2141	1; 3	1900
19 May 2013	Norman, OK	2300	4	1900
20 May 2013	Moore, OK	1956	5	1800
31 May 2013	El Reno, OK	2305	3	2100
27–28 Apr 2014	Central AR	0006	4	2000
28 Apr 2014	MS–AL outbreak	2051	4	1800
11 May 2014	NE tornado	2050	3	1900

more thorough analysis of whether combining satellite and radar data will be useful and where further research is required to prevent forecast degradation from unwanted interactions between the two datasets.

Section 2 provides a brief overview of the satellite data and retrieval algorithm. Section 3 describes the experiment design and the CWP forward operator. Section 4 describes observation diagnostics for each case while section 5 discusses the differences between radar-only and radar with satellite data experiments for selected analysis and forecast times. Finally, section 6 provides concluding remarks.

2. Observations

Observations from three different platforms are assimilated in these experiments. For Oklahoma-centric and Arkansas cases, surface observations from the Oklahoma Mesonet (McPherson et al. 2007) including temperature, dewpoint, wind velocity, and pressure are assimilated. All experiments assimilate radar reflectivity and radial velocity from three radars within the individual experiment domain. The mesonet and radar datasets are described in detail in Part I and in previous ensemble data assimilation studies such as those of Yussouf et al. (2013), Jones et al. (2015), and Wheatley et al. (2014). Observations from the GOES satellites are added as part of this research to assess their potential for improving storm-scale forecasts compared to assimilating primarily radar data observations.

The GOES Imager takes multispectral (visible and infrared) images over the continental United States every 5–15 min (Menzel and Purdom 1994; Schmit et al. 2001). Cloud properties are retrieved from 4-km-resolution GOES Imager radiances for pixels classified as cloudy using the multispectral retrieval algorithm known as the visible infrared shortwave-infrared split-window technique (VISST; Minnis et al. 2011). The CO_2-absorption technique of Chang et al. (2010) is also used in the retrieval of cloud-top pressure (CTP) for thin cirrus clouds. Cloud-base pressure (CBP) is the pressure corresponding to the altitude equal to the difference between cloud-top height and cloud thickness. Cloud thickness is estimated with a parameterization that depends on the cloud temperature, optical depth, and cloud water path (Minnis et al. 2010).

The cloud-phase algorithm classifies a cloudy pixel as being either ''liquid'' or ''ice'' based on the cloud-top temperature and cloud effective particle size information. Optically thick clouds containing both liquid- and ice-phase hydrometeors are generally classified as ice clouds since the current iteration of the retrieval algorithm is unable to separately classify mixed-phase clouds (Minnis et al. 2007). Hereafter, liquid water path (LWP) refers to the cloud water path associated with liquid-phase clouds only while ice water path (IWP) refers to the cloud water path for ice- and mixed-phase clouds. CWP is used when discussing both LWP and IWP simultaneously. A full description of the VISST algorithm can be found in Minnis et al. (2011). The observation error is defined as a function of both LWP and IWP values with the lowest errors defined for clear-sky retrievals, and the highest for thick and precipitating clouds similar to those used in Jones et al. (2015) (Table 2).

Figures 1a and 1b show the visible and infrared channel images from *GOES-13* at approximately 2030 UTC on 19 May 2013 over Oklahoma with the corresponding retrievals for LWP, IWP, CTP, and CBP. The visible image shows a linear band of broken stratus and cumulus clouds extending from north Texas into southern Kansas. These are generally classified as liquid-phase clouds with LWP values generally less

TABLE 2. Observation errors for IWP and LWP defined as a function of the retrieval value.

IWP/LWP (kg m^{-2})	Error (kg m^{-2})
<0.025	0.025
0.025–0.2	0.05
0.2–0.5	0.075
0.5–1.0	0.10
1.0–2.5	0.15
>2.5	0.25

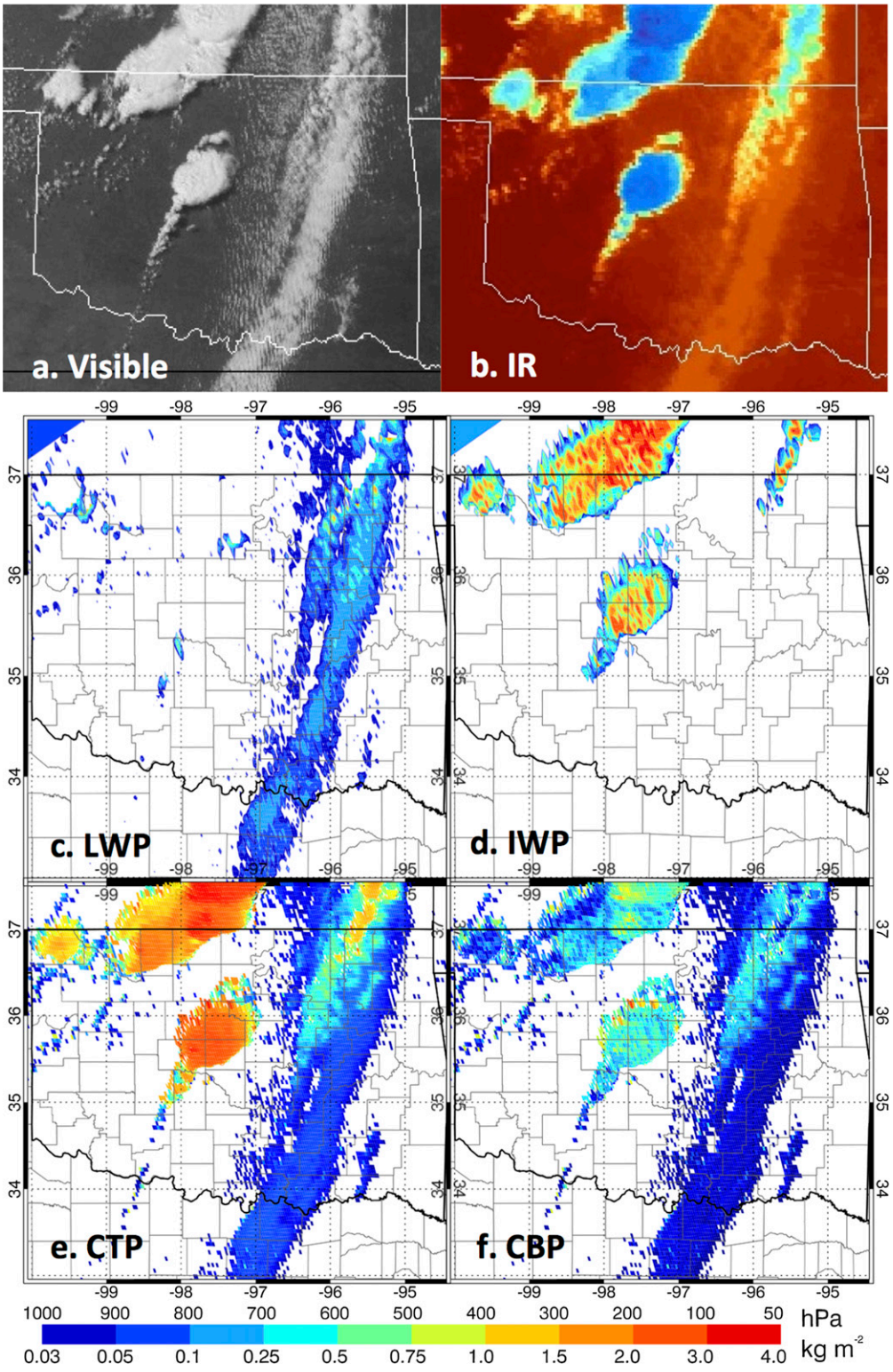

FIG. 1. *GOES-13* (a) visible and (b) infrared satellite imagery over OK at 2030 UTC 19 May 2013. Note the developing convection in central OK and the band of low-level clouds to the east. (c) LWP, (d) IWP, (e) CTP, and (f) CBP retrievals for 2030 UTC. Note that the developing convection is high topped and classified as ''ice'' and the eastern band of clouds is lower topped and classified as ''liquid.''

than 0.5 kg m^{-2} and CTP below 600 hPa (Fig. 1c). Cirrus from ongoing convection is present in northwestern Oklahoma and southern Kansas and developing convection is present along a dryline in central Oklahoma. These are generally classified as ice-phase clouds and have IWP in excess of 1.0 kg m^{-2} with corresponding cloud-top pressures above 200 hPa (Fig. 1e). CBP is also higher even in the storm cores where clouds actually extend from near the surface to the top of the troposphere. This is a result of the uncertainties in the cloud thickness parameterization for the thickest clouds.

Satellite retrievals are smoothed to a 6-km grid prior to assimilation similar to the resolution of the assimilated radar observations; however, the satellite and radar data remain on different grids. This smoothing removes unwanted variations like those seen in Fig. 1c for IWP and also produces a dataset better suited to a 3-km model using the "2 Δx" guideline described by Lu and Xu (2009). For tall clouds, geolocation errors exceeding 10 km can occur; thus, a parallax correction is applied where clouds exist. The geolocation of the raw satellite data and retrievals measures the physical condition of the cloud at its top and not its base, and since the satellite is not directly overhead, the relative locations at the surface and aloft are not the same. To correct for parallax, the retrieved cloud height is used to remap cloudy pixels to their zenith location above the surface (Wang and Huang 2014).

The impacts of assimilating CWP retrievals have been described in detail by Jones et al. (2013b, 2015) and Jones and Stensrud (2015). In summary, assimilating CWP retrievals associated with cloud cover increases the hydrometeor and moisture concentrations in the model state generating clouds features within the model where none are present. Depending on cloud height and thickness, these features can include low-level stratus fields and upper-level cirrus outflow associated with strong convection. Assimilating high values of IWP associated with developing convection also generates a "warm bubble" in the midtroposphere that acts to further sustain and grow convection in favorable environments (Jones and Stensrud 2015). Assimilating cloud-free retrievals acts to reduce hydrometeor and moisture concentrations and has the effect of removing spurious cloud cover. The impact on the cloud analyses directly impacts the radiation budget in the model since the amount of incoming solar and outgoing longwave radiation is changed. The radiation schemes within the model adjust the thermodynamic state to better reflect this new radiation balance. Assimilating retrievals alone was generally able to develop and sustain convection within the model for both real-case and idealized simulations (Jones et al. 2013b). However, the lack of 3D hydrometeor and velocity information often resulted in analyzed storms having a poor organization, which requires that radar reflectivity and radial velocity data also be assimilated to produce an accurate representation of convection within the model.

3. Experiment design

a. NEWS-e

This research uses the ensemble data assimilation system described in detail in Part I. In summary, this version of the NEWS-e uses the Advanced Research version of the Weather Research and Forecasting Model (WRF-ARW), version 3.4.1 (Skamarock et al. 2008), to generate storm-scale analyses and forecasts for the six severe weather events shown in Table 1 using a 36-member ensemble. Radar and satellite data are assimilated using the parallel ensemble adjustment Kalman filter (EAKF) approach in the Data Assimilation Research Testbed (DART) software system (Kalman 1960; Anderson 2001; Anderson and Collins 2007; Anderson et al. 2009) using a configuration similar to that employed by Wheatley and Stensrud (2010), Yussouf et al. (2013), and Jones et al. (2013a, 2015).

The experimental domain utilizes a one-way nest setup, whereby the parent and nested grids are run concurrently with information only exchanged at the lateral boundaries at 1-h intervals once storm-scale data assimilation commences (with no feedback from the nested grid to the parent grid). The parent grid has a horizontal gridpoint spacing of 15-km covering the continental United States, while the nested grid has a horizontal gridpoint spacing of 3 km whose location is event dependent. Both parent and nested domains have 51 vertical levels ranging from the surface to a model top of 10 hPa. Initial conditions for the parent and nested grids are downscaled from the 21-member 0000 UTC Global Ensemble Forecast System (GEFS) forecast cycle. The GEFS also provides boundary conditions for the parent grid. Different sets of WRF model physics options are applied to each ensemble member to account for model physics uncertainties (e.g., Stensrud et al. 2000; Fujita et al. 2007; Meng and Zhang 2008; Wheatley et al. 2014; Part I) (Table 3). To maintain ensemble spread, the spatially and temporally varying adaptive inflation [Anderson (2007, 2009); DART namelist options: inf_initial = 1.0, inf_sd_initial = 0.8, inf_damping = 0.9, inf_lower_bound = 1.0, inf_upper_bound = 100, inf_sd_lower_bound = 0.8] is applied to the prior ensemble estimate at the outset of each assimilation step. All members use Thompson's cloud microphysics scheme (Thompson et al. 2004, 2008), and

TABLE 3. Multiphysics options applied to the GEFS ensemble members to initialize ensemble members 1–18 of the NEWS-e. This set of physics options also is applied to the same GEFS ensemble members, in reverse order, to initialize ensemble members 19–36 of the NEWS-e. All ensemble members use Thompson cloud microphysics and the RAP land surface model. All parameterizations are as in Part I.

	Parameterizations			
			Radiation	
Member	Cumulus	PBL	Shortwave	Longwave
1	Kain–Fritsch	YSU	Dudhia	RRTM
2		YSU	GCM version of the Rapid Radiative Transfer Model (RRTMG)	RRTMG
3		MYJ	Dudhia	RRTM
4		MYJ	RRTMG	RRTMG
5		Mellor–Yamada–Nakanishi–Niino (MYNN)	Dudhia	RRTM
6		MYNN	RRTMG	RRTMG
7	Grell	Yonsei University (YSU)	Dudhia	RRTM
8		YSU	RRTMG	RRTMG
9		MYJ	Dudhia	RRTM
10		MYJ	RRTMG	RRTMG
11		MYNN	Dudhia	RRTM
12		MYNN	RRTMG	RRTMG
13	Tiedtke	YSU	Dudhia	RRTM
14		YSU	RRTMG	RRTMG
15		MYJ	Dudhia	RRTM
16		MYJ	RRTMG	RRTMG
17		MYNN	Dudhia	RRTM
18		MYNN	RRTMG	RRTMG

no cumulus parameterization is applied on the storm-scale grid.

The mesoscale ensemble is integrated hourly, assimilating conventional observations (Mesonet, METAR, marine, radiosonde, ACARS, and satellite winds). Horizontal and vertical localization radii of ~458 km and 6 km, respectively, are applied using the Gaspari and Cohn (1999) technique. Available mesonet observations are only assimilated in the storm-scale domain using a smaller localization radius of 60 km. Data assimilation on the mesoscale grid ceases when assimilation of radar and satellite data on the storm-scale grid begins. The rationale for this decision comes from the planned real-time implementation of this system. The latency for most conventional observations is 30 min or longer, which means they are not available for data assimilation system cycling at 15-min intervals. The exception to this is Oklahoma Mesonet data, which are provided at 5-min intervals with a latency of 5 min or less. Storm-scale data assimilation of radar and satellite observations begins near the time of the issuance of the first severe weather watch associated with each event. Generally, this occurs an hour or more prior to the development of the first reported tornado. For some cases, the start time occurs prior to convective initiation while for others strong convection is ongoing in the domain.

Radar and satellite data assimilation cycles at 15-min intervals on the storm-scale grid until the tornadic event has ended or until 0000 UTC, whichever comes first. Reflectivity and radial velocity are assimilated using a horizontal localization radius of 18 km with a vertical localization radius of 6 km. Both conventional and radar observations use an outlier threshold of three standard deviations from the prior ensemble mean. For both mesoscale and storm-scale grids, the updated model state includes 3D wind components, potential temperature, geopotential height, atmospheric pressure, water vapor, diabatic heating, the cloud microphysics hydrometeor mixing ratios and number concentrations, and finally radar reflectivity.

b. *Satellite forward operator*

The forward operator and satellite data assimilation techniques are described in detail by Jones et al. (2013b) and Jones et al. (2015). In summary, predicted LWP and IWP results are calculated at each assimilation cycle using the column-integrated cloud hydrometeor mixing ratio. For each grid point and model level, the mixing ratios of each hydrometeor variable (q_c, q_r, q_i, q_s, and q_g) are summed to form a total cloud water mixing ratio q_a. For mixed-phase clouds, the total cloud water mixing ratio is then integrated over the entire atmospheric

column and divided by the gravitational acceleration constant to calculate the predicted IWP value. A similar value q_{liq} is generated from only the liquid-phase hydrometeors for comparison with LWP retrievals. For all clouds, the vertical observation height of the cloud layer at each observation location is defined by the average of CTP and CBP with a 6-km vertical localization radius applied surrounding the center of the cloud. Clear-sky (CWP = 0 kg m^{-2}) retrievals are also assimilated except that the vertical observation height and localization radius remain undefined. Both cloudy and clear-sky retrievals have a horizontal localization radius of 40 km applied. A larger six standard deviation outlier threshold is applied when assimilating retrievals. Testing showed that using a larger outlier threshold for satellite retrievals proved more effective than using the more restricted threshold of three standard deviations.

Unlike Jones et al. (2015), this initial real-time data observation processing system was fashioned in such a way that removing CWP observations in heavy precipitation regions was not practical, potentially leading to underestimates of CWP in these areas. Comparisons of GOES satellite CWP retrievals to *CloudSat* radar data indicate that the retrieval algorithm significantly underestimates CWP for deep convective clouds (Smith 2014). To partially compensate for this, the CWP forward operator includes hard limits for the prior and posterior ensemble mean LWP and IWP. The limits are 4.5 kg m^{-2} for IWP and 3.5 kg m^{-2} for LWP, which roughly correspond to the maximum possible retrieval values. In heavy precipitation regions, the prior ensemble mean IWP or LWP and the corresponding observation will have similar values and while the observation will be assimilated, its impact will be small as a result of the small innovation resulting from the limits in the forward operator. However, differences in the distribution of LWP and IWP between retrievals and model output can still result in some biases remaining even after application of the limits defined above.

Both satellite and radar observations are correlated with the hydrometeor characteristics of the atmosphere. While satellite observations are more sensitive to nonprecipitating clouds and radar observations are more sensitive to those that are precipitating, their observations and corresponding observation errors are not completely independent of each other. As a result, assimilating satellite and radar observations at the same location may not always be beneficial. For example, if radar observations indicate precipitation in an area where the satellite retrieval indicates a low CWP cloud, it is likely that the resulting model analysis where both are assimilated will underestimate the actual precipitation. If radar data indicate light or no precipitation where high CWP retrievals occur, then a positive bias in precipitation is likely to result. Future research will analyze potential data-thinning strategies to reduce these apparent biases present in the current model configuration.

The radar-only (RAD) experiments described in Part I assimilate positive reflectivity, clear-air (0 dBZ) reflectivity, and radial velocity from the three WSR-88Ds that provide the greatest coverage over the storm-scale domain. This research compares the RAD experiments for each event to similar experiments that assimilate LWP, IWP, and clear-sky (CWP = 0 kg m^{-2}) observations in addition to positive reflectivity and radial velocity. The RADSAT experiments do not assimilate clear-air reflectivity since one goal of this research is to replace 3D clear-air reflectivity observations with a much smaller number of 2D satellite cloud-free observations. Both observation types act to decrease hydrometeor and moisture concentrations in the model analysis; however, assimilating multiple clear-air reflectivity observations in a clear-sky environment can result in an unwanted dry bias in the model analysis. Assimilating a single satellite-derived cloud-free observation still removes anomalous precipitation and cloud cover, but does not repeatedly ''hit'' the model at a particular location, reducing the potential dry biases. In addition, not assimilating clear-air reflectivity reduces the overall number of observations by 50%, resulting in an assimilation that runs up to 50% faster. The increase in model performance can make the difference in whether or not 15-min cycling can be accomplished in real time with reasonable computing resources. Still, clear-air reflectivity can be useful where clouds exist in thin layers to prevent the model from overdeveloping these clouds into precipitation. To test this hypothesis, clear-air reflectivity is assimilated into two extra experiments (RAD0SAT) for the 19 May and 27 April events.

4. Observation diagnostics

To assess how radar and satellite observations are being assimilated, observation diagnostics in the form of mean innovation (e.g., bias), root-mean-square innovation (RMSI), and total spread (TSPRD) are calculated for LWP and IWP retrievals at each assimilation cycle (Dowell et al. 2004; Dowell and Wicker 2009; Dowell et al. 2011; Yussouf et al. 2013; Part I). Innovation and RMSI are calculated by taking the difference between prior and posterior fields $H(x)$ and comparing against observations y:

$$\text{Innov} = y_n - H(x_n) \quad \text{and} \tag{1}$$

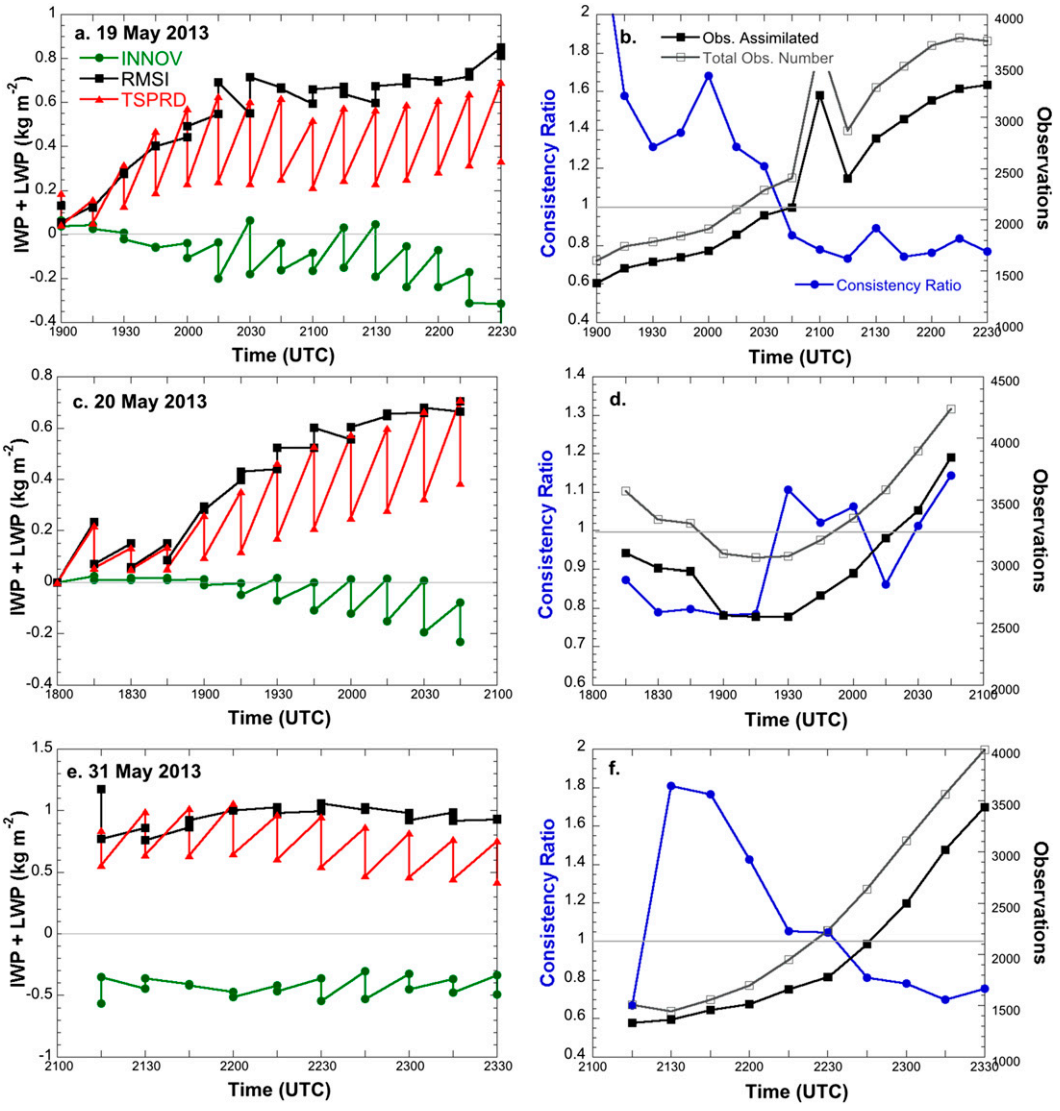

FIG. 2. The 2013 innovation, RMSI, TSPRD, and CR for LWP + IWP at 15-min intervals during the assimilation period for the (a),(b) 19 May, (c),(d) 20 May, and (e),(f) 31 May 2013 events. Also present are the total number of observations available at each assimilation cycle and the number of those that are actually assimilated.

$$\mathrm{RMSI} = \sqrt{\left(\sum_{n=0}^{N} \mathrm{Innov}_n\right)^2 \Big/ N}, \qquad (2)$$

where N represents the number of observations assimilated for a particular observation type.

Ensemble spread represents the average difference between the individual ensemble forecasts of a quantity and the ensemble forecast of a quantity:

$$\mathrm{SPRD} = \sqrt{\frac{1}{E-1}\sum_{e=1}^{E}[H(x_e) - \overline{H(x)}]^2}, \qquad (3)$$

where E is the total number of ensemble members.

Total variance is the sum of the prior ensemble variance plus the observation error variance for each observation type whose square root defines the TSPRD. The consistency ratio (CR) represents the ratio of prior ensemble variance RMSI^2 to the square of TSPRD. A CR near 1.0 indicates that the ensemble variance is a good approximation of the error variance for a given observation error (Dowell et al. 2004; Aksoy et al. 2009; Dowell and Wicker 2009). Small CR values indicate an ensemble with insufficient spread, while large CR values indicate an ensemble with excessive spread due to larger than optimum observation errors.

CR, innovation, RMSI, and TSPRD are provided at each assimilation cycle for IWP and LWP observations for the 2013 events in Fig. 2. The number of available

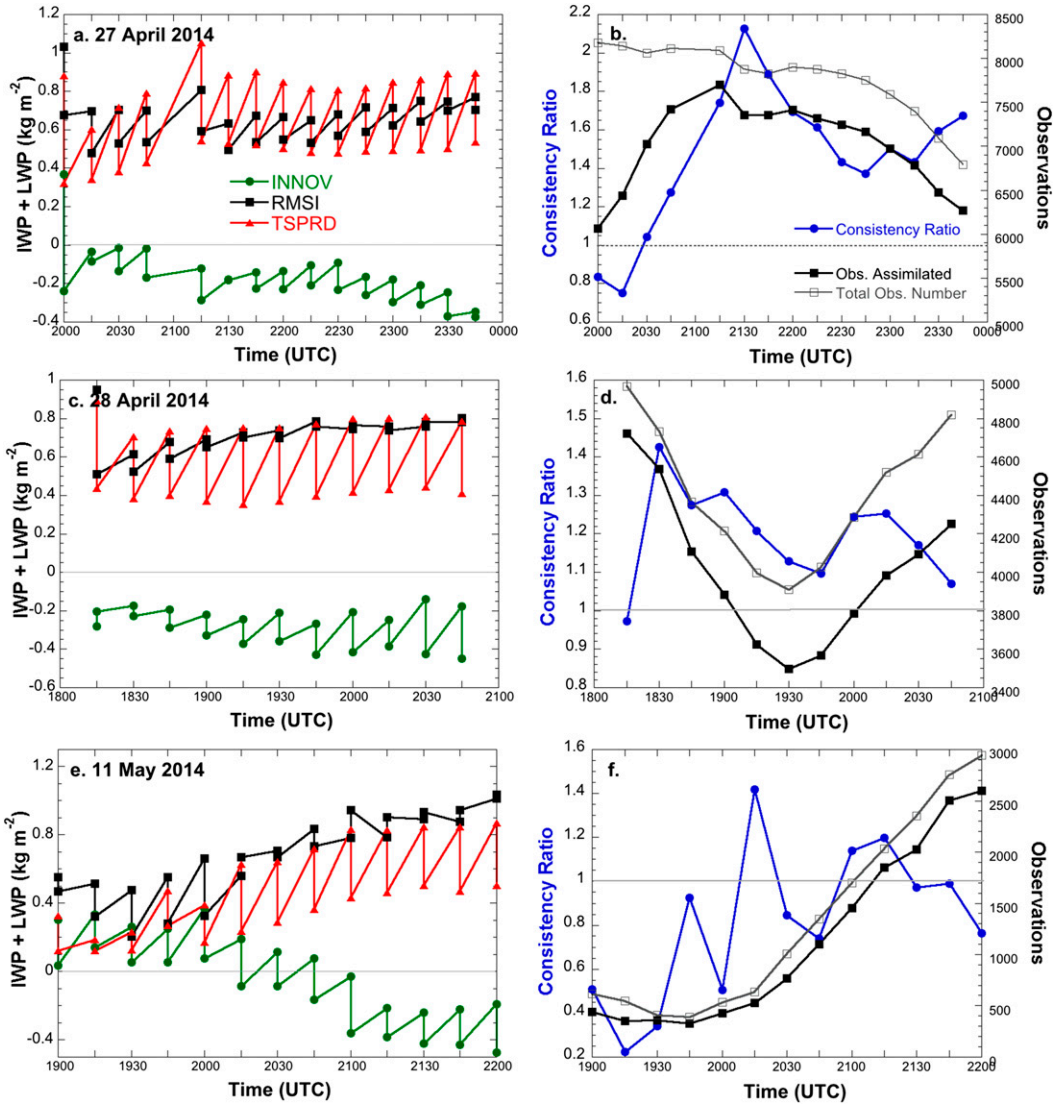

FIG. 3. As in Fig. 2, but for the 2014 events. Note that the 11 May event does not assimilate LWP data.

observations and the subset of those that are assimilated are also provided. For the 19 and 20 May events, RMSI increases from near zero and eventually stabilizes near a value of $0.6\,\mathrm{kg\,m^{-2}}$ after 2 h of data assimilation (Figs. 2a,c). TSPRD shows a similar increase as a function of time. The mean innovation slowly decreases, indicating that as storms develop and become more widespread, the forecast LWP and IWP from the model are higher than the retrieved observations despite the limits included in the forward operator for model-simulated LWP and IWP values. The 31 May case is similar, but generates a relatively constant innovation, RMSI, and TSPRD as a function of time (Fig. 2e). After ~2 h of data assimilation, the CR stabilizes at greater than 0.6 for the 19 and 31 May events and to between 0.8 and 1.1 for the 20 May event (Figs. 2b,d,f). For all 2013 events, between 85% and 90% of available observations pass outlier threshold tests and are assimilated.

Figure 3 shows the corresponding statistics for the three 2014 cases. In general, the same trends are apparent with one major exception. At the beginning of the 27 April event, only 75% of the total number of observations are assimilated during the first cycle at 2000 UTC (Fig. 3b). The total percent of available observations assimilated increases to near 90% by 2130 UTC, but CR increases to near 2.0 at the same time before decreasing to only 1.4 afterward, corresponding to excess spread. These statistics indicate that model cloud features and the observations differ significantly at 2000 UTC and, while the assimilation

does close this gap, the differences remain, potentially leading to adverse effects on the model forecasts. It should be noted that only IWP data are assimilated into the 11 May case because of a processing error discovered in that event's LWP retrievals. Thus, the number of observations for this case begins at a low number and increases as the anvils associated with the developing storms become larger (Fig. 3f). For all cases, the impacts to reflectivity and radial velocity observation diagnostics are small when satellite retrievals are assimilated. The total spread for the reflectivity increases by approximately 10% while little change occurs for radial velocity.

5. Selected analyses and forecasts from each event

Since it would be impossible to discuss every analysis and forecast generated as part of this research, a single analysis time and the corresponding 1-h forecasts initiated from those times that are generally representative of the event are discussed in detail.

a. 19 May 2013

Two violent tornadoes were generated from two separate supercells on 19 May (Table 1). The first storm (No. 1) generated a weak tornado at ~2120 UTC followed by a much stronger tornado beginning at 2141 UTC. Ensemble mean 2-m temperatures for each experiment are provided in Fig. 4 showing very warm air in western Oklahoma behind the dryline with cooler surface temperatures to the east. The impacts of assimilating satellite data are apparent when comparing surface temperature between experiments. RADSAT and RAD0SAT generate warmer temperatures in northeast Texas and southeast Oklahoma at 2045 UTC (Figs. 4a–c). These differences are a result of the changes in cloud characteristics within the model due to the assimilation of the satellite data. These changes can be visualized using the downward shortwave flux variable (SWDOWN), which is a measure of the amount of solar radiation reaching the surface. High values indicate clear-sky conditions while lower values indicate the presence of clouds, at least during daylight hours. This variable is also measured by the Oklahoma Mesonet, but is not assimilated, allowing for an independent comparison of the model to observations. Large differences in SWDOWN are evident between the RAD and RADSAT experiments. The cloud shield associated with the central Oklahoma storm is also too small, as indicated by the low SWDOWN observations on the south side of this storm. The corresponding *GOES-13* visible image also shows a larger anvil than present in RAD while showing few clouds in northeast Texas and central Oklahoma (Fig. 4g). Both RADSAT and RAD0SAT match the SWDOWN observations and visible imagery much better than does RAD (Figs. 4b,c,e,f,g). The cloud cover in northeast Texas is removed, allowing for the warmer surface temperatures. Also, the linear band of clouds ahead of the storm is evident in the SWDOWN analysis for these experiments. Overall, the addition of clear-air reflectivity does not cause large changes to the surface temperature and SWDOWN compared to RADSAT. However, RAD0SAT does return the smaller anvil size present in the RAD experiment. The impact of assimilating both cloud-free satellite observations and clear-air reflectivity is to increase the influence of ''clear'' observations relative to ''cloud'' observations, decreasing the cloud fields along the edges of the storms.

Since Oklahoma Mesonet observations are available at 5-min intervals, it is possible to quantitatively compare surface temperature and SWDOWN analyses and forecasts with observations at each forecast interval, providing a quantitative estimate of the impacts of assimilating satellite data. Root-mean-square errors (RMSEs) for temperature and SWDOWN were computed over 105 mesonet sites in the domain for each member and forecast time. The mean and standard deviation of RMSE were then computed. The standard deviation of RMSE represents the degree of spread present in the forecast from member to member. It should be noted that the standard deviation of the RMSE is not necessarily an indicator of statistical significance. To assess RMSE over multiple forecast periods, the RMSE for forecasts initiated between 2030 and 2200 UTC at 15-min intervals were averaged at a particular forecast time, creating a single time series for RMSE. Standard deviation was averaged in the same manner to provide an overall estimate of spread. Figures 5a and 5b show surface temperature and SWDOWN RMSEs as functions of forecast time for the RAD, RADSAT, and RAD0SAT experiments. For surface temperature, the RMSE for RAD increases from 1.3°C at the analysis time to near 3.0°C after 1 h, with the overall standard deviation also increasing to over ±1.0°C. RADSAT and RAD0SAT begin with a slightly higher RMSE, but the increase as a function of time is much less than for RAD maxing out below 2.5°C. The standard deviations are also much smaller, indicating that the variability in surface temperature among members is much smaller once LWP and IWP are assimilated. Adding clear-air reflectivity, which is present in both cloudy and cloud-free areas, had little impact on the surface temperature errors. RAD also generates the highest RMSEs for SWDOWN with the RADSAT RMSEs being 20–40 $W m^{-2}$ lower for all

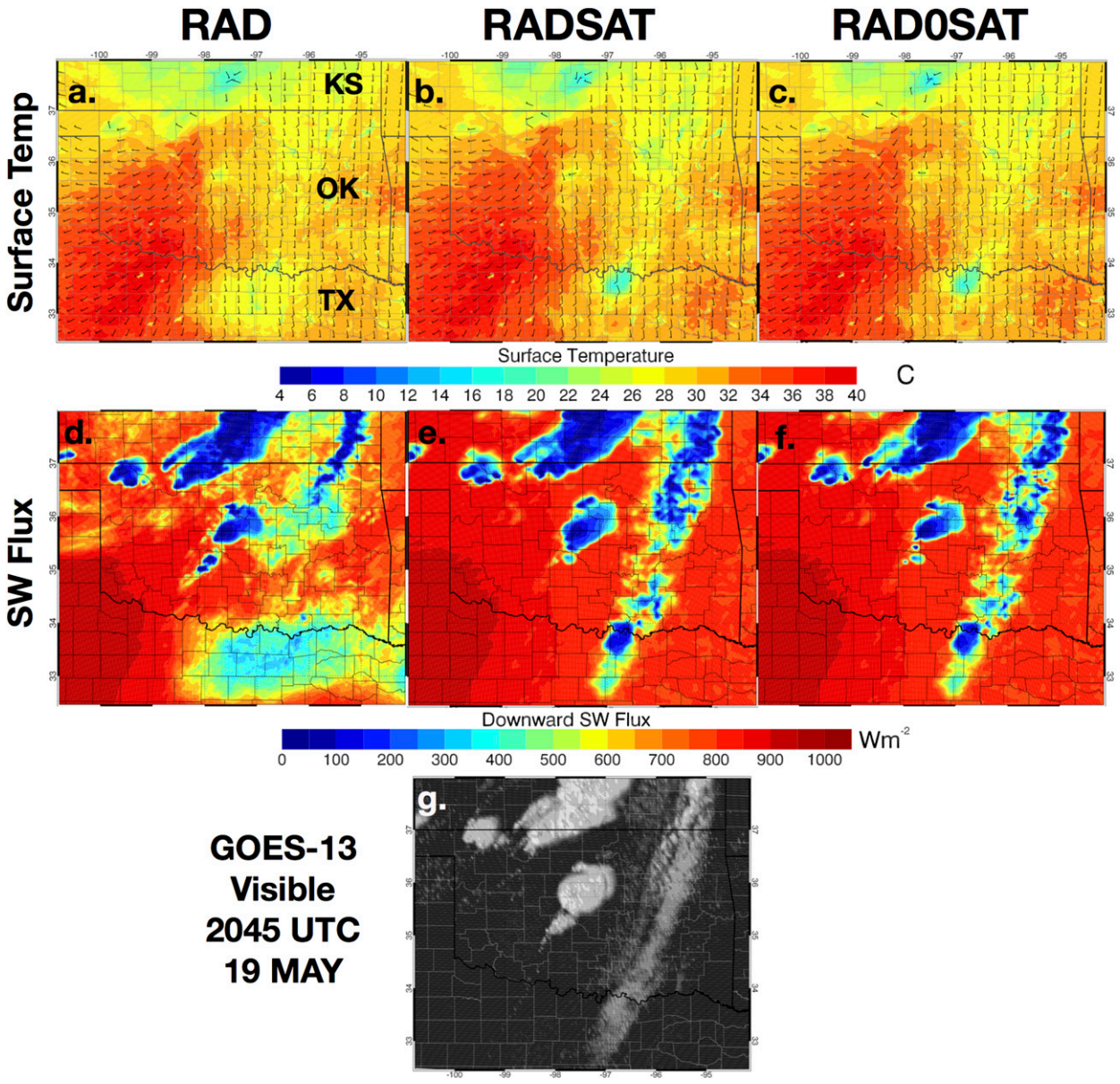

FIG. 4. Ensemble mean (a)–(c) 2-m surface temperature and (d)–(f) downward shortwave flux analyses for RAD, RADSAT, and RAD0SAT experiments at 2045 UTC 19 May. (g) *GOES-13* visible at this time is provided for comparison. Wind barbs are plotted on the surface temperature panels with values of 5 m s^{-1} indicated by short barbs and values of 10 m s^{-1} indicated by long barbs. If wind speed is less than 5 m s^{-1}, then no barbs are plotted.

forecast times (Fig. 5b). The standard deviation or RMSE is also greater for RAD, but not to the degree it is for surface temperature. RAD0SAT generates RMSEs for SWDOWN approximately 10 W m^{-2} higher than does RADSAT, which is consistent with the reduction in cloud cover due to assimilating both cloud-free satellite data and precipitation-free observations at the same locations.

The large differences in the thermodynamic and cloud properties of each experiment are likely to influence the forecasting of storms within the model. Each experiment generates a good match between the ensemble mean 3 km above ground level (AGL) reflectivity and the 3 km AGL reflectivity from the multiradar, multisensor (MRMS) product indicated by the 40-dB*Z* observation contour at 2045 UTC (Figs. 6a–c). RAD has the best match while RADSAT is similar near the storm cores, but also generates areas of spurious reflectivity in regions where clouds exist, indicating the overproduction of light precipitation (not shown).

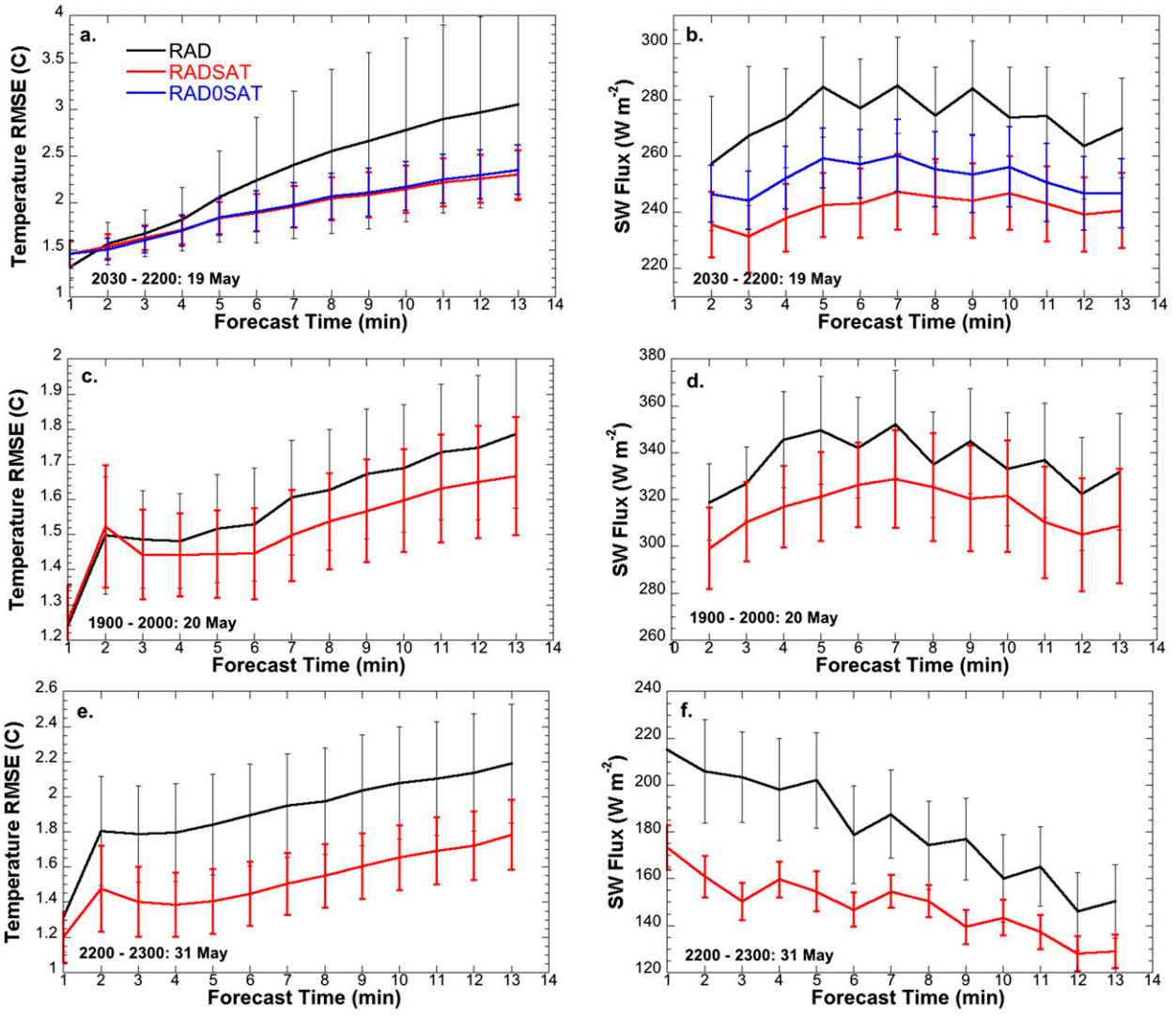

FIG. 5. RMSE for ensemble 2-m surface temperature and downward shortwave flux for five sets of 1-h forecasts (seven for 19 May) for (a),(b) 19 May, (c),(d) 20 May, and (e),(f) 31 May 2013 verified against OK Mesonet observations. Error bars indicate standard deviation of RMSE over each ensemble member for a particular forecast time.

Introducing clear-air reflectivity eliminates the spurious precipitation, but also appears to weaken the smaller storms in the domain. The differences between the experiments become even more apparent 30 min into the forecast at 2115 UTC. RADSAT generates higher ensemble mean reflectivity compared to RAD for both areas of convection while the spurious precipitation in RADSAT has disappeared (Figs. 6d,e). Conversely, RAD0SAT weakens the central Oklahoma storm significantly (Fig. 6f). By 60 min into the forecasts (2145 UTC), corresponding to near the time of the touchdown of the violent tornado, all experiments forecast a storm somewhat north of the observations, with RADSAT having the highest reflectivity and RAD0SAT having the lowest (Figs. 6g–i).

To indicate the location of low-level rotation occurring within forecast convection, the probability of maximum vertical vorticity $> 0.004\,s^{-1}$ below 2 km AGL is computed for the 1-h forecast period. These probabilities represent the fraction of ensemble members in which the vertical vorticity exceeds $0.004\,s^{-1}$ on at least one model level below 2 km AGL at a given time and horizontal grid point as defined by Part I. Vorticity fields are first calculated at the ensemble analysis time used to initialize the forecast, and at 5-min intervals thereafter through the forecast end time. The maximum probability recorded at each horizontal grid point is shown for forecasts initiated at 2045 UTC for each experiment in Figs. 6j–i. In central Oklahoma, each experiment places the

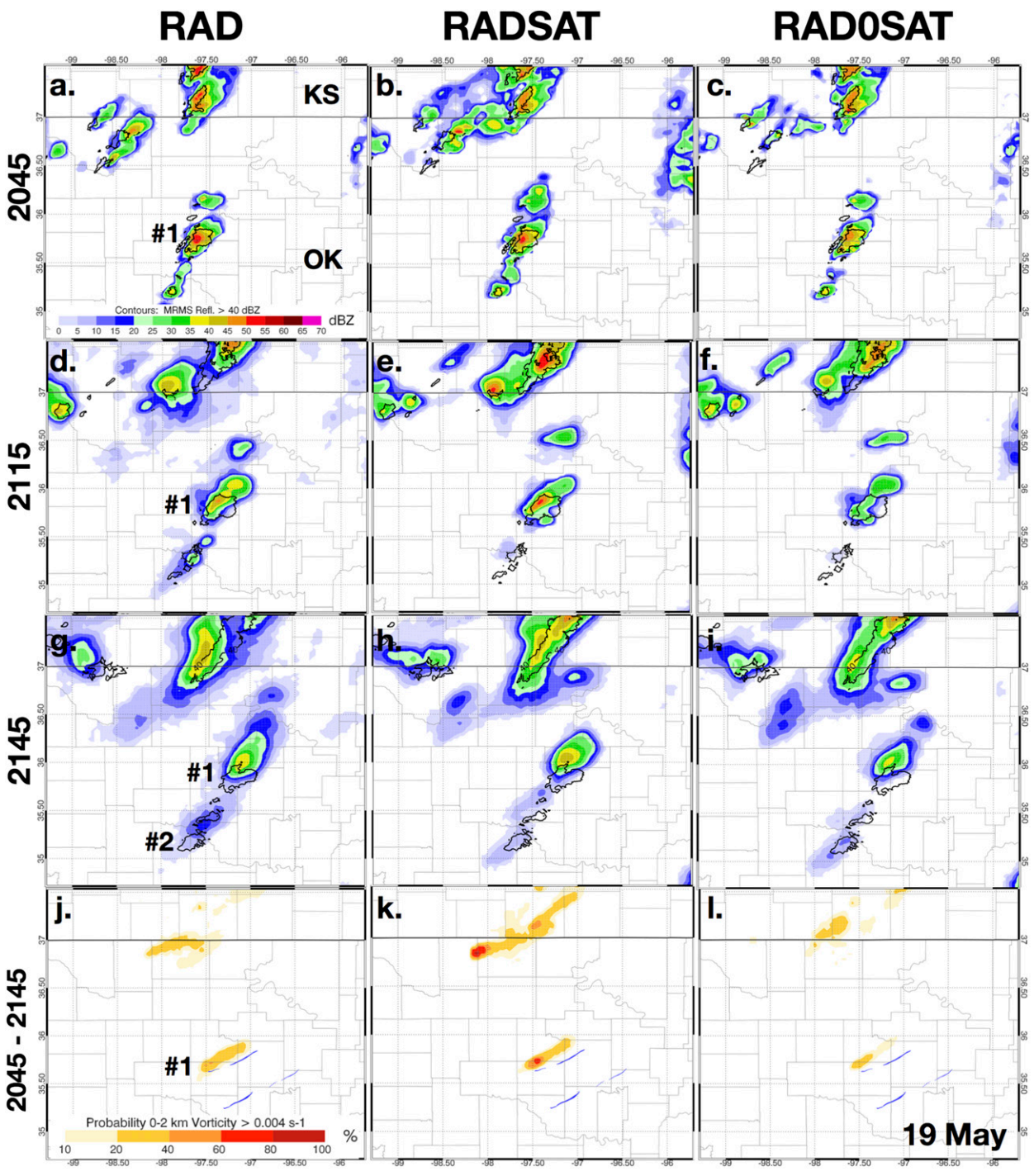

FIG. 6. Ensemble mean 3 km AGL reflectivity at 2045 UTC 19 May 2013 for (a) RAD, (b) RADSAT, and (c) RAD0SAT experiments. The (d)–(f) 30-min and (g)–(i) 1-h ensemble mean 3-km reflectivities are provided. The black contour indicates area where MRMS 3-km radar reflectivity $>$ 40 dBZ at the analysis or forecast time. Probability of 0–2-km vertical vorticity $>$ 0.004 s^{-1} for 0–1-h forecasts initiated at 2045 UTC 19 May for the (j) RAD, (k) RADSAT, and (l) RAD0SAT experiments. Blue lines indicate known tornado tracks in the area.

highest probability of low-level vorticity along and to the north of the tornado track denoted by the blue outline associated with storm 1. RADSAT generates somewhat higher vorticity probabilities than RAD, with both having similar tracks (Figs. 6j,k). RAD0SAT generates the lowest probabilities, consistent with the weaker reflectivity forecasts described above.

While the qualitative comparisons of reflectivity and vorticity between the experiments indicate that assimilating satellite observations improves the forecast of supercell convection, it is also important to assess this question in a quantitative manner. The bias (ratio of the number of yes observations to yes forecasts) and equitable threat score (ETS; Wilks 2006) are computed for the ensemble mean 3 km AGL reflectivity averaged over 1-h forecasts initiated every 15 min between 2030 and 2200 UTC 19 May for the RAD, RADSAT, and RAD0SAT experiments. For each member, if the experiment generates reflectivity greater than 40 dBZ within ±3 km of the MRMS reflectivity greater than 40 dBZ at a particular time, this is considered a "hit." If the experiment generates reflectivity greater than 40 dBZ and this threshold is not exceeded in the observations, then it is considered a false detection. Finally, if neither the observations nor the experiment exceed this threshold, then it is considered a correct null forecast. The goal is to generate forecasts where hits are maximized, but false detections are limited. The mean and standard deviation of bias and ETS among each member are then computed for each forecast time. Finally, the bias and ETS mean and standard deviation for a particular forecast time are averaged for all sets of experiments to create a time series of bias and ETS results that reflects the skill over multiple forecast periods.

For all experiments, ETS generally decreases as a function of time as model error increases (Fig. 7a). Much of the decrease in skill is due to the increasing displacement error between the location of the forecast convection and reflectivity observations. Both RADSAT and RAD0SAT maintain higher ETS scores throughout the entire forecast period with the greatest improvements occurring for 30–60-min forecasts. The advantage of RADSAT increases over time as persistence plays a decreasing role and the importance of thermodynamic conditions related to cloud coverage increases. Assimilating satellite observations affects these conditions by increasing or decreasing the cloud cover in the model, which has downstream impacts on atmospheric moisture content and temperature. Corresponding bias statistics for the same set of forecasts are shown in Fig. 7b with both RADSAT and RAD0SAT generating values significantly less than 1.0, indicating an overall underforecast by these experiments. RAD generates average biases nearer to 1.0, but the variability in bias as a function of ensemble members is much greater compared to RADSAT and RAD0SAT. These statistics indicate that RAD is generating additional grid points greater than 40 dBZ when compared with the other experiments. However, they are displaced from and potentially not associated with any observed convection.

b. 20 May 2013

Similar atmospheric conditions that generated the 19 May tornadoes remained in place over central Oklahoma on 20 May and generated another round of tornadic storms. This event produced a violent tornado in Moore, Oklahoma, that touched down at approximately 1956 UTC and continued on an eastward path for approximately 40 min (Table 1). This storm formed at the intersection of a dryline and weak frontal boundary, which increased its low-level shear compared to other storms farther south. The ensemble mean surface temperature ~40 min prior at 1915 UTC indicates warm air and westerly winds in southwestern Oklahoma with cooler air to the north and east (Figs. 8a,b). Both RAD and RADSAT generate similar overall features, but some differences are apparent. First, RADSAT is warmer in northeast Texas compared to RAD, where generally cloud-free conditions exist (Fig. 8e). As occurred for the 19 May event, RAD is generating spurious cloud cover in this region as shown by the decrease in SWDOWN compared to RADSAT (Figs. 8c,d). Another difference occurs in eastern and northeastern Oklahoma, where a band of cooler surface temperatures exists in RADSAT. This cool band is associated with a band of clouds observed in the visible imagery that is assimilated into this experiment. RAD fails to correctly analyze this feature since radar observations alone cannot provide information on nonprecipitating clouds.

Surface temperature and SWDOWN RMSE are calculated and averaged over forecasts initiated at 1900, 1915, 1930, 1945, and 2000 UTC (Figs. 5c,d). RADSAT generates the lowest surface temperature RMSE 10 min into the forecast period. However, the overall improvement remains small, on the order of 0.1 K. Standard deviations among the ensemble members are also similar for both experiments (0.2°C), which differs from the 19 May experiments where the temperature standard deviation for RAD increases rapidly compared to RADSAT. RADSAT also decreases SWDOWN RMSE on the order of 20 W m^{-2} compared to RAD, further indicating that the assimilation of LWP and IWP is improving the overall cloud properties in the model analysis leading to better forecasts of these clouds and the corresponding near-surface thermodynamic conditions.

Ensemble mean 3-km reflectivity at 1915 UTC shows several developing supercells (Figs. 9a,b). Storm 1 goes on to produce the Moore tornado at 1956 UTC while storm 2 generates a couple of brief, weak tornadoes soon after the analysis time. Both experiments correctly

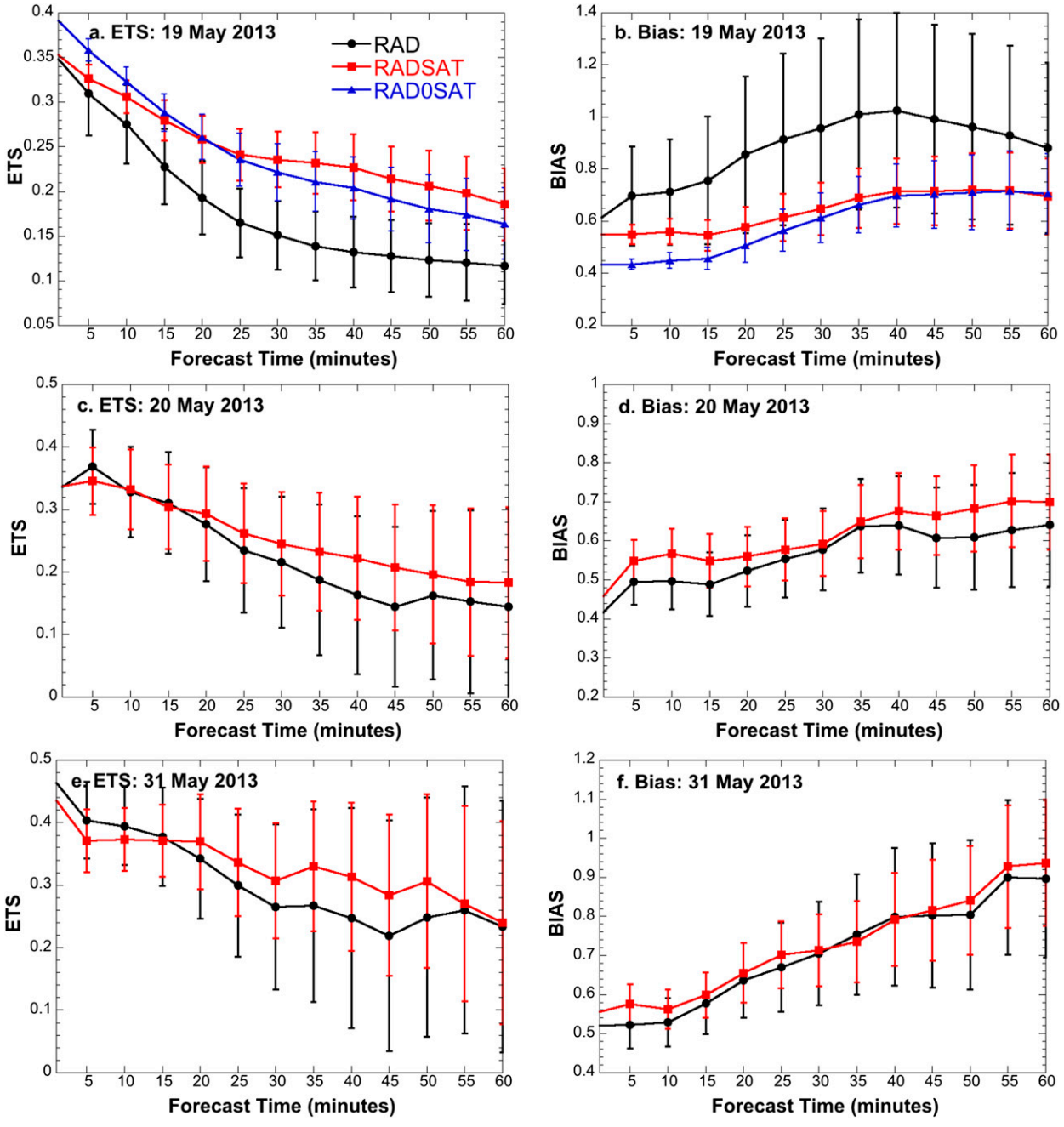

FIG. 7. (left) ETS and (right) bias for 3 km AGL ensemble mean reflectivity forecasts compared to 3 km AGL MRMS reflectivities calculated for the 2013 events. Bias and ETS shown represents the average bias and ETS for five (seven for 19 May) sets of 0–1-h forecast periods to evaluate model performance over a multiple forecast initiation times. Error bars indicate standard deviation of ETS over each ensemble member for a particular forecast time.

analyze the primary storm cores, with RADSAT generating slightly higher reflectivity values for storm 1 (Fig. 9b). RADSAT maintains higher ensemble mean reflectivity 30 min into the forecast at 1945 UTC for both storms (Figs. 9c,d). The higher ensemble mean reflectivity generated by RAD remains at 2015 UTC (Figs. 9e,f). Finally, RADSAT appears to better analyze a developing storm in the southern portion of the domain.

The differences between the 0- and 2-km vorticity probability swaths from RAD and RADSAT are consistent with the reflectivity forecasts described above.

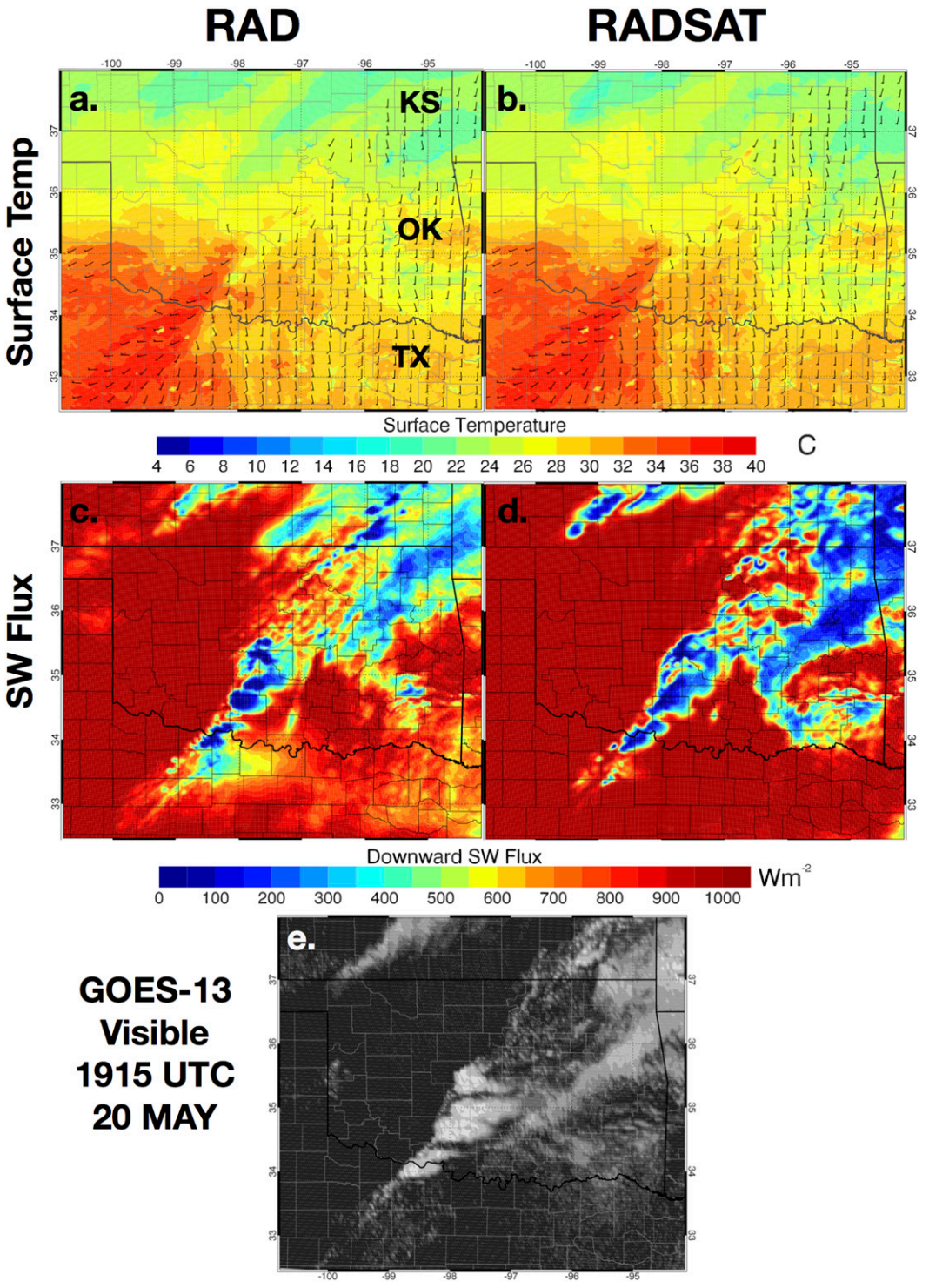

FIG. 8. Ensemble mean (a),(b) 2-m surface temperature and (c),(d) downward shortwave flux for the RAD and RADSAT experiments at 1915 UTC 20 May. (e) *GOES-13* visible at this time is provided for comparison. Otherwise, as in Fig. 4.

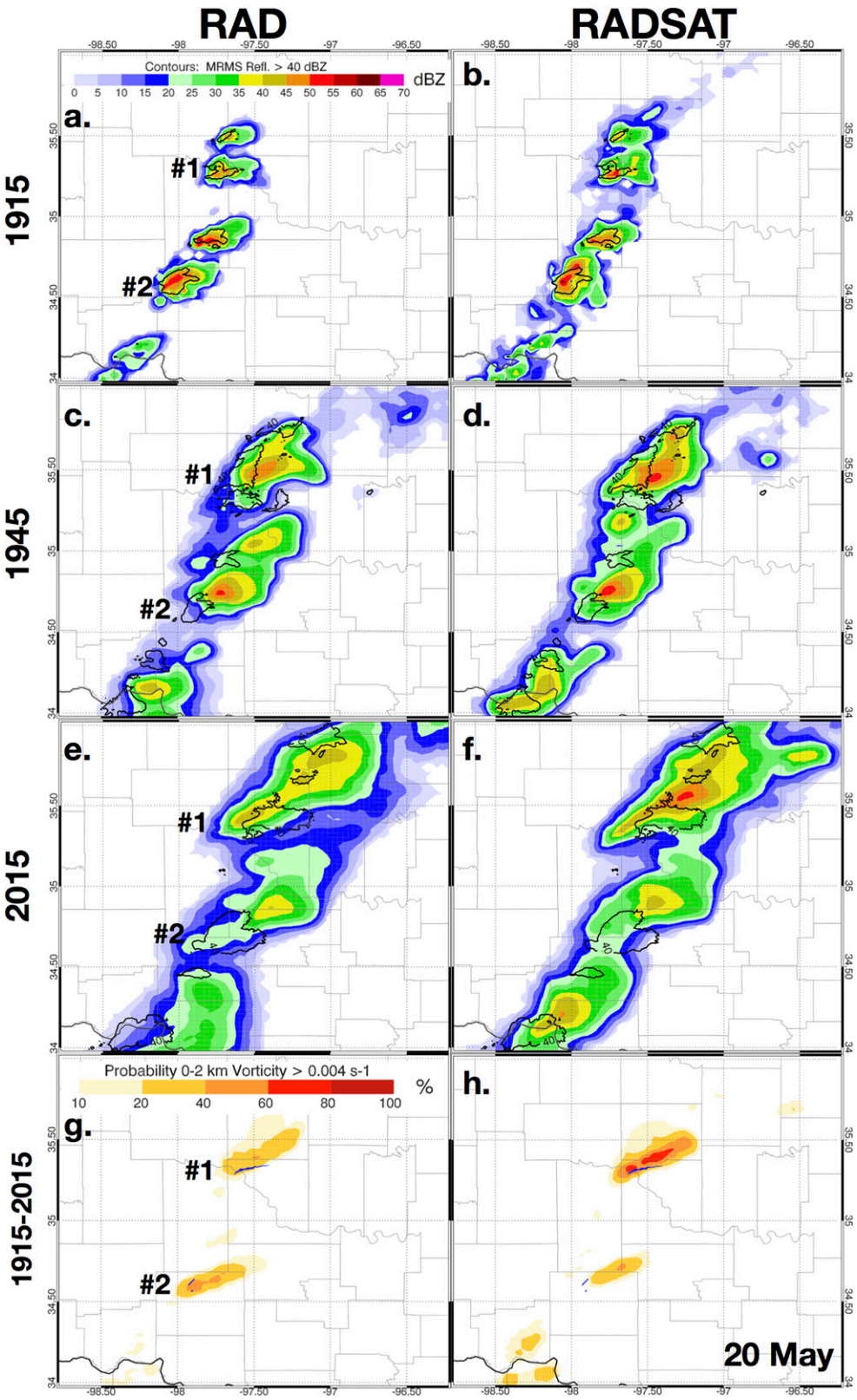

FIG. 9. Ensemble mean 3 km AGL reflectivity at 1915 UTC 20 May 2013 for (a) RAD and (b) RADSAT experiments. The (c),(d) 30-min and (e),(f) 1-h ensemble mean 3-km reflectivities are provided. Otherwise, as in Fig. 6.

RAD only generates a 40% or less probability of 0–2-km vorticity greater than $0.004\,s^{-1}$ whereas RADSAT generates probabilities in excess of 60% for storm 1 (Figs. 9g,h). Conversely, RAD generates slightly higher probabilities for storm 2 during the first 15 min of the forecast period with both experiments being similar afterward. One potential explanation for this result is that storm 2 is better organized in RAD at the analysis time, but the organization rapidly improves in RADSAT as a result of the impacts of assimilating satellite observations outside the storm cores.

ETS and bias skill scores for 3-km reflectivity were computed for forecasts started at 1900, 1915, 1930, 1945, and 2000 UTC 20 May and averaged for each forecast time (Figs. 7c,d). At forecast times beyond 15 min, RADSAT generates higher ETS scores compared to RAD, which is consistent with the qualitative discussion above. Both experiments generate a low bias indicating underforecasting, with RAD generating slightly lower biases and greater overall variability compared to RADSAT.

c. 31 May 2013

The 31 May event was characterized by a very large tornado that began at 2305 UTC associated with the southernmost supercell in a storm complex that developed in central and north-central Oklahoma (Table 1). One hour prior to the development of the tornado at 2200 UTC, very warm surface temperatures are analyzed in western Oklahoma and north Texas with cooler conditions to the east (Figs. 10a,b). Larger differences are apparent in the SWDOWN analysis with RAD generating much lower values across much of eastern Oklahoma compared to RADSAT where visible satellite imagery indicates only sporadic cloud cover (Figs. 10c–e). The decreased coverage of clouds in RADSAT reduces surface temperature RMSE for 1-h forecasts generated starting at 1900, 1915, 1930, 1945, and 2000 UTC by approximately 0.4°C over much of the forecast period (Fig. 5e). The overall standard deviation of RMSE is also slightly smaller, but not to the degree observed in the 19 May experiment. RADSAT also generates smaller RMSEs for SWDOWN compared to RAD, consistent with the other cases (Fig. 5f). Overall, SWDOWN RMSE decreases as a function of time as the magnitudes of SWDOWN begin to decrease as the sun sets, reducing the overall shortwave flux reaching the surface.

Important differences are also apparent when comparing RAD and RADSAT reflectivity forecasts. Figure 11 shows ensemble mean 3-km reflectivity analyzed at 2200 UTC and for 30-min and 1-h forecasts at 2230 and 2300 UTC, respectively, for both experiments. Both experiments correctly analyze the location of strong convection, with RADSAT generating some excess light precipitation along the edges. However, RADSAT generates higher ensemble mean reflectivity 30 min into the forecast with several values greater than 50 dBZ present (Figs. 11c,d). The same pattern continues to 2330 UTC with the main storm being well maintained by both experiments and RADSAT generating some spurious convection to the south (Figs. 11e,f). Both experiments generate moderate to high probability of 0–2-km vorticity greater than $0.004\,s^{-1}$ west of and along the future tornado track and forecast the southeastern turn that occurred with this storm just prior to the formation of the tornado. The primary difference between the experiments is that RADSAT generates vorticity probabilities greater than 80% over a well-defined swath whereas RAD generates only a few small areas of probability greater than 60% and is also stronger with the left split to the north. RADSAT does generate several small moderate-probability vorticity swaths to the south of the primary storm corresponding to the stronger storms apparent in the reflectivity forecasts. The spurious convection in southern Oklahoma is a result of IWP associated with towering cumulus being assimilated, introducing a convective initiation signal into the model. Since RADSAT does not assimilate clear-air reflectivity, no mechanism exists to suppress this signal.

The ETS and bias for 3-km reflectivity averaged over forecasts initiated at 2200, 2215, 2230, 2245, and 2300 UTC 31 May show a pattern similar to the previous events (Figs. 7e,f). Both experiments generate high ETS scores (>0.4) at the analysis time and decrease thereafter. RAD performs slightly better during the first 15 min of the forecast period, while RADSAT performs better for the remainder of the forecast period. However, the standard deviation in ETS is quite large and like the 20 May event, significant overlap in the ensemble distribution of ETS exists between both experiments. Biases are similar for both experiments and slowly increase with time, indicating a model that initially underforecasts reflectivity, but improves in storm coverage as time goes on.

d. 27 April 2014

The 27 April and following 28 April events are more characteristic of lower instability, high vertical wind shear events often found outside the southern plains (Table 1). On 27 April, several areas of severe convection were present in eastern Oklahoma, and central and northern Arkansas. The storm-scale data assimilation period begins at 2000 UTC, during which significant convection is ongoing within the domain, unlike the isolated convective cases from 2013. A supercell present in west-central Arkansas generated a violent tornado at 0006 UTC.

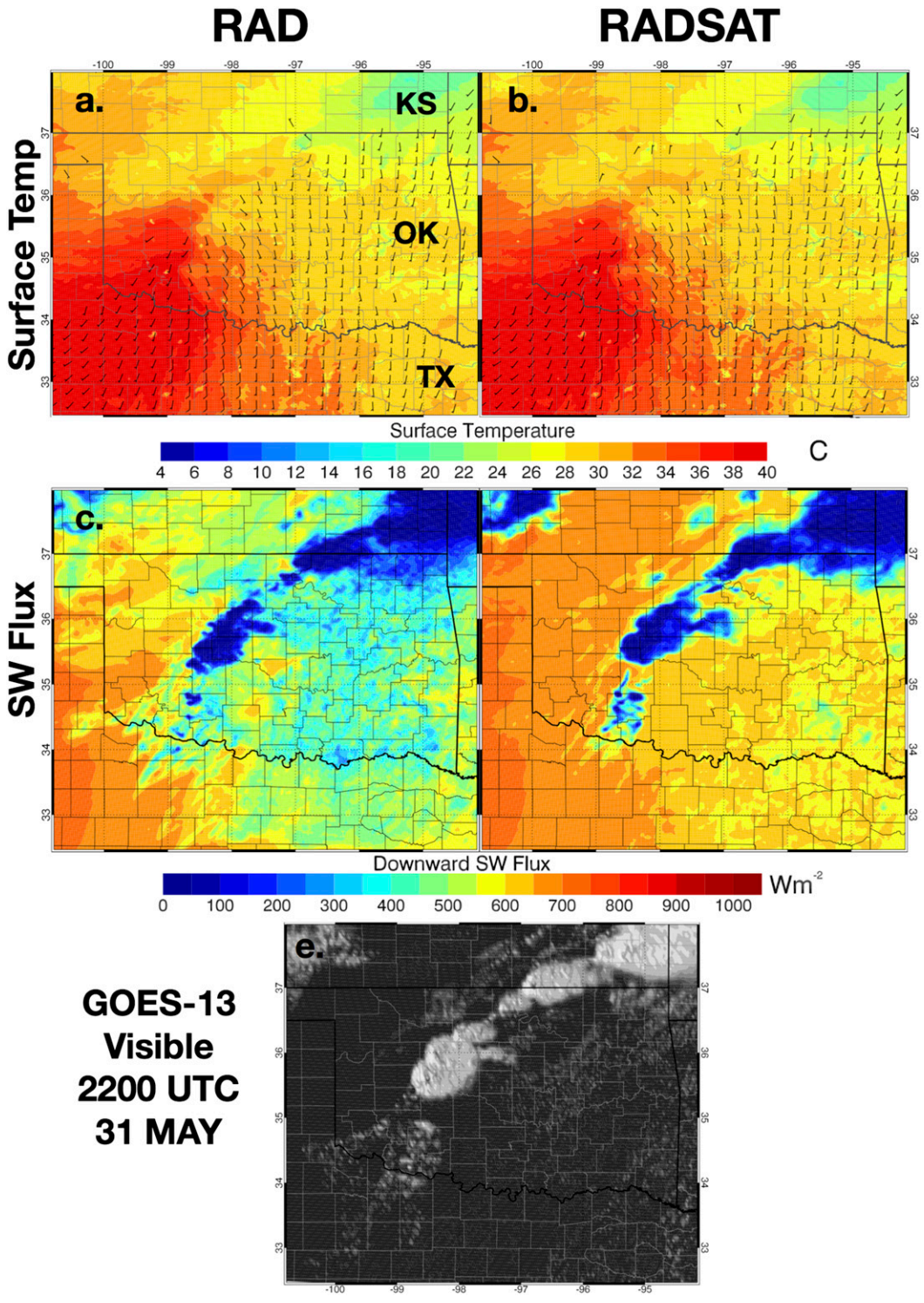

FIG. 10. As in Fig. 8, but for 2200 UTC 31 May 2013.

Surface temperature analyses at 2330 UTC for both the RAD and RADSAT experiments show a large area of less than 20°C temperatures in northwestern Oklahoma and southern Missouri associated with ongoing precipitation. The RAD0SAT experiment that assimilates clear-air reflectivity along with satellite observations was also run for this event and generates similar surface temperatures as RADSAT (Figs. 12a–c). The differences

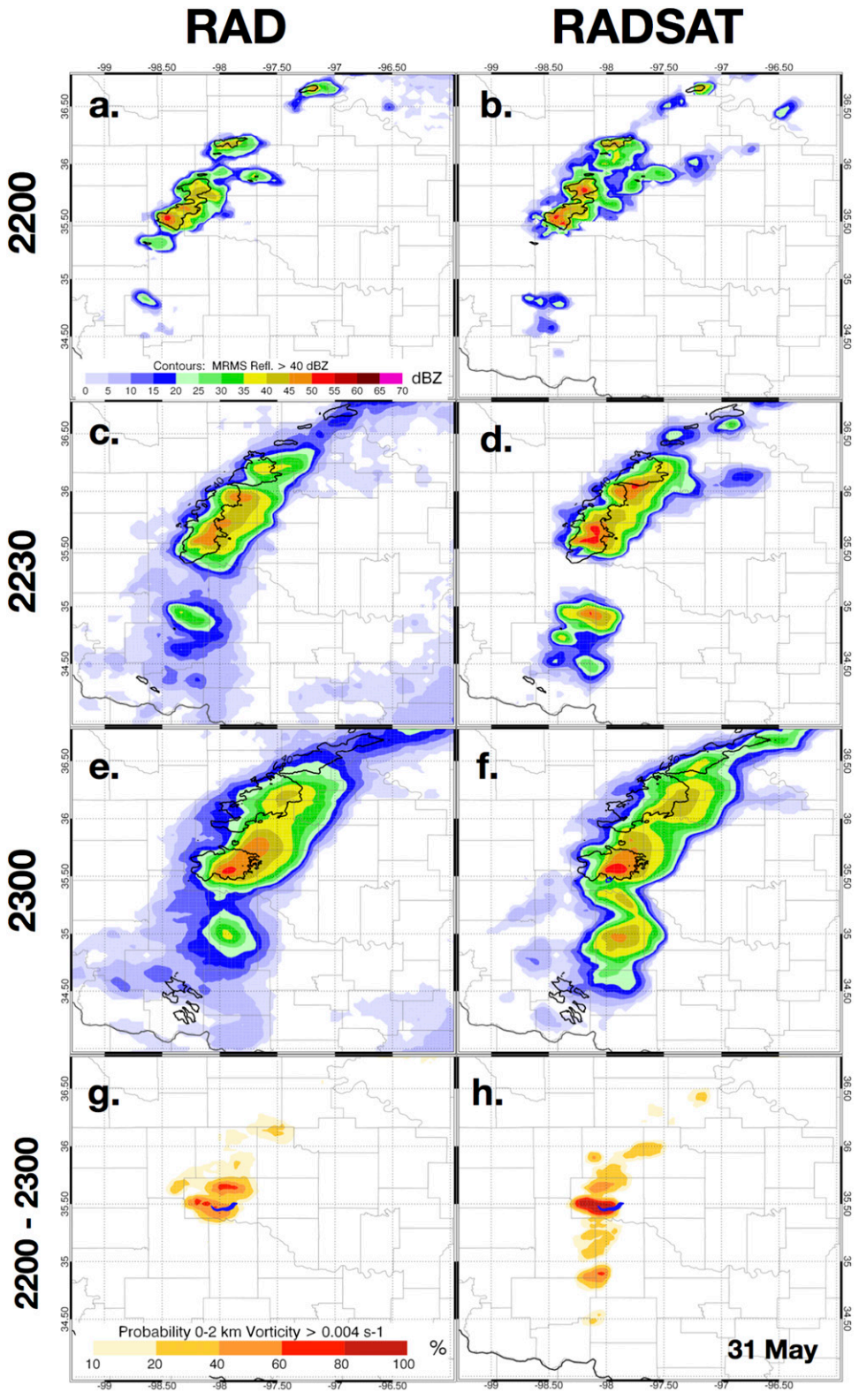

FIG. 11. As in Fig. 9, but for forecasts initiated at 2200 UTC 31 May 2013.

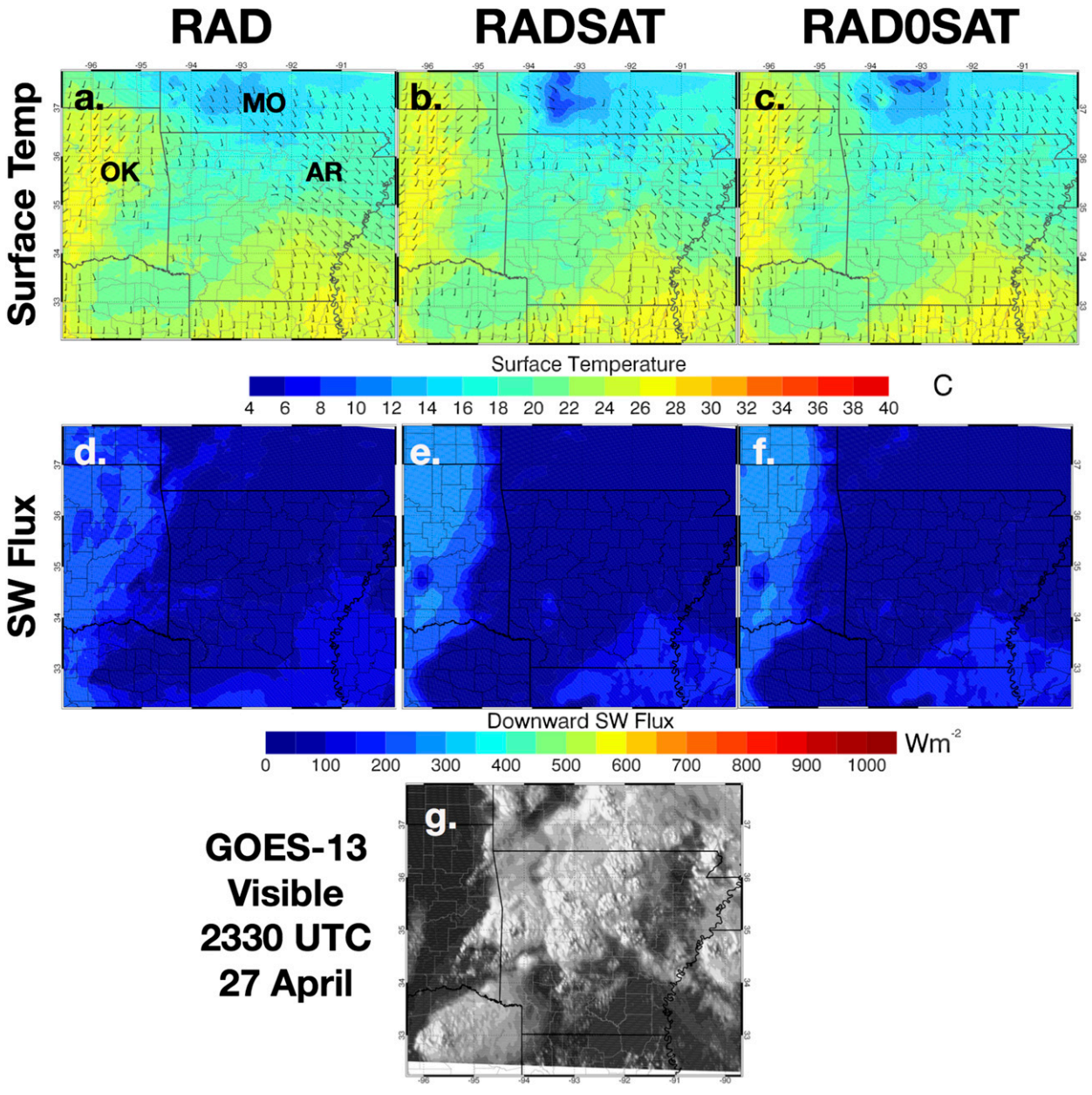

FIG. 12. As in Fig. 4, but for 2330 UTC 27 Apr 2014.

between the experiments, especially in Arkansas, are generally small. Somewhat larger differences exist in the SWDOWN analysis with RADSAT (and RAD0SAT) better analyzing the clear sky behind the ongoing convection (Figs. 12d–f). RADSAT also appears to reduce cloud cover over southern Arkansas compared to RAD. The SWDOWN values for all experiments are much lower ($<300\,\mathrm{W\,m^{-2}}$) compared to the previous events since this event occurred earlier in the year and the analysis time is later, meaning much less incoming solar radiation. Qualitative comparison of the SWDOWN analyses with visible satellite imagery at the same times (Fig. 12g) indicates that from a cloud-coverage perspective, assimilating LWP and IWP improves the appearance of the initial cloud fields. Unfortunately, the spatial and temporal resolutions of available surface observations for this and the following 2014 events do not allow for quantitative comparisons similar to those conducted for the 2013 events.

Whether or not the differences in cloud coverage observed above lead to an improved forecast of severe convection can be determined by analyzing the forecast

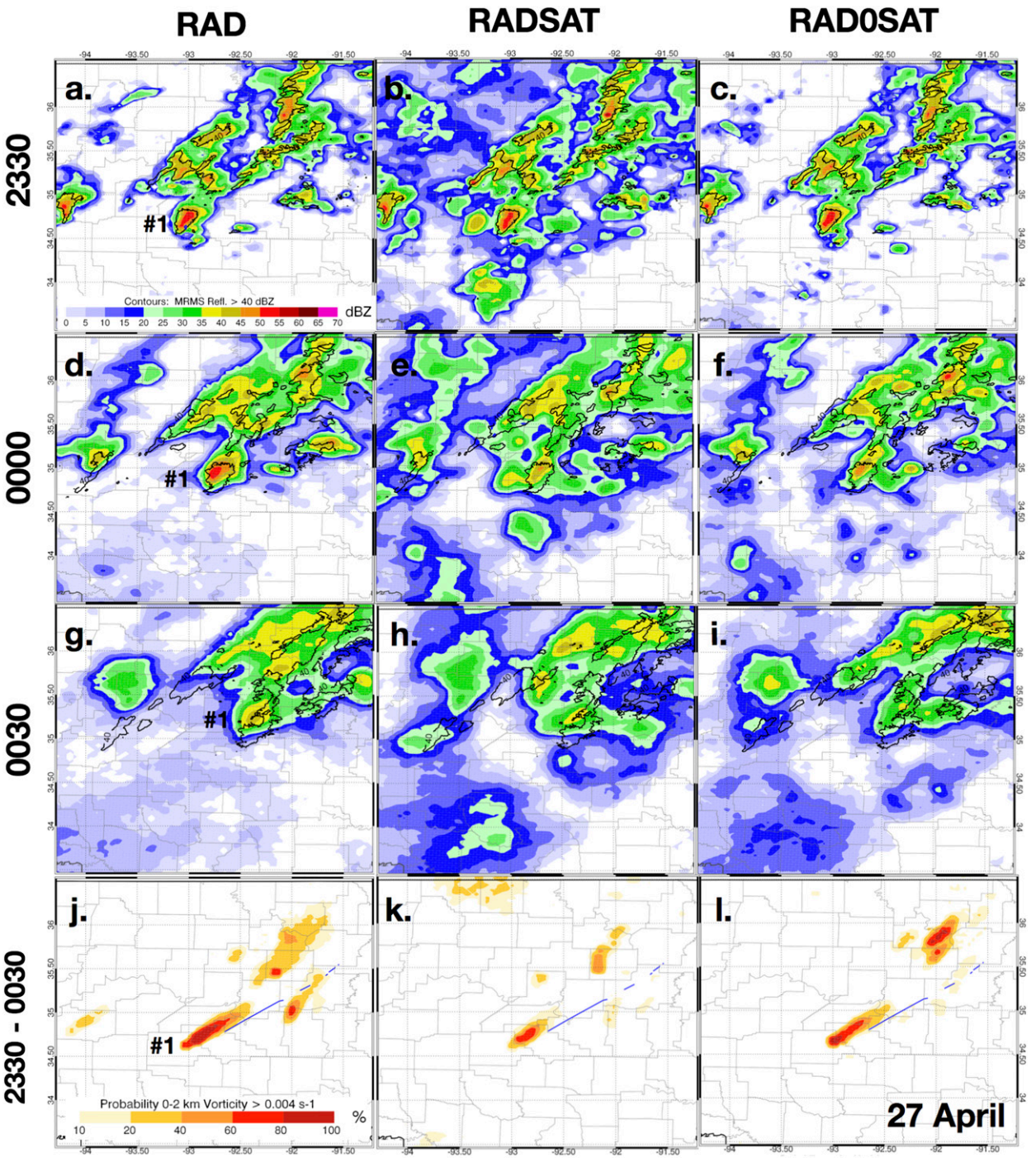

FIG. 13. As in Fig. 6, but for forecasts initiated at 2330 UTC 27 Apr 2014.

ensemble mean 3-km reflectivity at 2330 UTC and 30-min and 1-h forecasts thereafter (Fig. 13). All three experiments correctly analyze the location of the soon-to-be-tornadic supercell (storm 1) while also analyzing much of the other ongoing convection in the domain. RADSAT differs from RAD in that it generates much larger areas of light precipitation outside the storm cores and even a separate area of precipitation south of the supercell that is not present in RAD or reality (Fig. 13b). This entire area is covered by cirrus clouds that generate high IWP retrievals, which upon assimilation, act to increase moisture and hydrometeor

concentrations in the model analysis after each assimilation cycle, eventually leading to precipitation in the absence of an observation type such as clear-air reflectivity to suppress this impact. Returning clear-air reflectivity to the set of observations in RAD0SAT removes much of the spurious precipitation while maintaining the overall cloud coverage of RADSAT (Figs. 12c and 13c). RAD maintains a core of greater than 50-dBZ reflectivity 30 min into the forecast (Fig. 13d) that remains discrete after 1 h (Fig. 13g). Conversely, RADSAT quickly weakens this storm and it becomes hard to discern from the surrounding convection after 1 h (Figs. 13e,h). RAD0SAT does not do much better despite correctly reducing the light-to-moderate precipitation outside the observed areas of convection (Figs. 13f,i).

The probability of 0–2 km vorticity greater than $0.004\,s^{-1}$ also differs significantly between each experiment (Figs. 13j–l). RAD generates a long swath of probabilities greater than 60% southwest of the beginning of the tornado track with lower probabilities extending well into and slightly north of the tornado track. RADSAT generates a much smaller, and lower-probability, swath consistent with the poor ensemble mean reflectivity forecasts. The spurious precipitation is likely reducing model instability, hindering further development of the supercell in the model. RAD0SAT improves the vorticity swath significantly though it remains slightly weaker than the RAD experiment.

The 0–1-h averaged ETS initiated from 2300, 2315, 2330, 2345, and 0000 UTC is consistent with these observations: RADSAT generally weakened high-reflectivity regions faster than RAD, yielding a consistently lower ETS (Fig. 14a). RAD0SAT increases ETS values relative to RADSAT, but they remain below those generated by RAD. Corresponding bias statistics indicate that RADSAT produced larger areas of reflectivity greater than 40 dBZ compared to the other experiments (Fig. 14b). For both RADSAT and RAD0SAT, bias increases as a function of forecast time, while RAD only generates a small increase. The RADSAT and RAD0SAT biases are near 1.0 by the 1-h forecast time, but the location of the convection is incorrect, leading to large false alarm values (not shown).

e. 28 April 2014

A supercell located on the southern edge of a large convective complex generated a violent tornado in central Mississippi that touched down at approximately 2051 UTC and remained on the ground for approximately 1 h (Table 1). At 2045 UTC, both experiments analyze relatively cool surface temperatures corresponding to ongoing cloud cover and precipitation over much of northern Mississippi (Fig. 15). Overall, the difference in surface temperature between the experiments is small, with RADSAT being slightly cooler in central Mississippi and warmer to the south (Figs. 15a,b). Much larger differences are apparent in the SWDOWN analyses, with RADSAT generating higher values both behind and ahead of the ongoing convection (Figs. 15c,d). RAD appears to generate spurious cloud cover in what should be limited cloud cover regions as indicated by visible imagery at this time (Fig. 15e). Assimilating cloud-free satellite observations clearly has a large impact on the model cloud analysis. IWP observations are less important in this case, since the model is already generating high values on its own in areas of deep convection.

Three separate supercells are ongoing and are analyzed by both experiments at 2045 UTC (Figs. 16a,b). The tornadic supercell (storm 1) is the southernmost storm in the domain at this time. As with the 27 April event, RADSAT generates much more light precipitation in the areas surrounding the main storms since clear-air reflectivity is not being assimilated to suppress this activity. The ensemble mean 3-km reflectivity results for 30-min and 1-h forecasts beginning at 2045 UTC show that while both experiments maintain an isolated storm corresponding to the observations, RADSAT generates somewhat lower overall ensemble mean reflectivity (Figs. 16c–f). The 0–2-km vorticity swaths show a similar trend with both experiments generating greater than 80% probabilities just southwest of the tornado touchdown location. Probabilities decrease somewhat faster in RADSAT, which is consistent with the lower ensemble mean reflectivity generated. Interestingly, RADSAT performs better with the developing convection in the southwestern potion of the domain at the 1-h forecast time by generating higher reflectivity values near the locations of the observed storms while most members of RAD fail to generate reflectivity greater than 35 dBZ in this region. ETS results averaged for 1-h forecasts initiated at 2000, 2015, 2030, 2045, and 2100 UTC show that RAD has slightly higher skill for the first 20 min of the forecast period, while RADSAT is higher for longer forecasts (Fig. 14c). RADSAT generates a somewhat higher bias, consistent with the greater coverage of precipitation observed in the forecasts (Fig. 14d).

f. 11 May 2014

The final event analyzed as part of this study occurred on 11 May 2014 in Nebraska during which a tornadic supercell rapidly developed along a frontal boundary generating a weak tornado at 2036 UTC and a much stronger tornado beginning at 2050 UTC (Table 1). This supercell eventually grew into a mesoscale convective

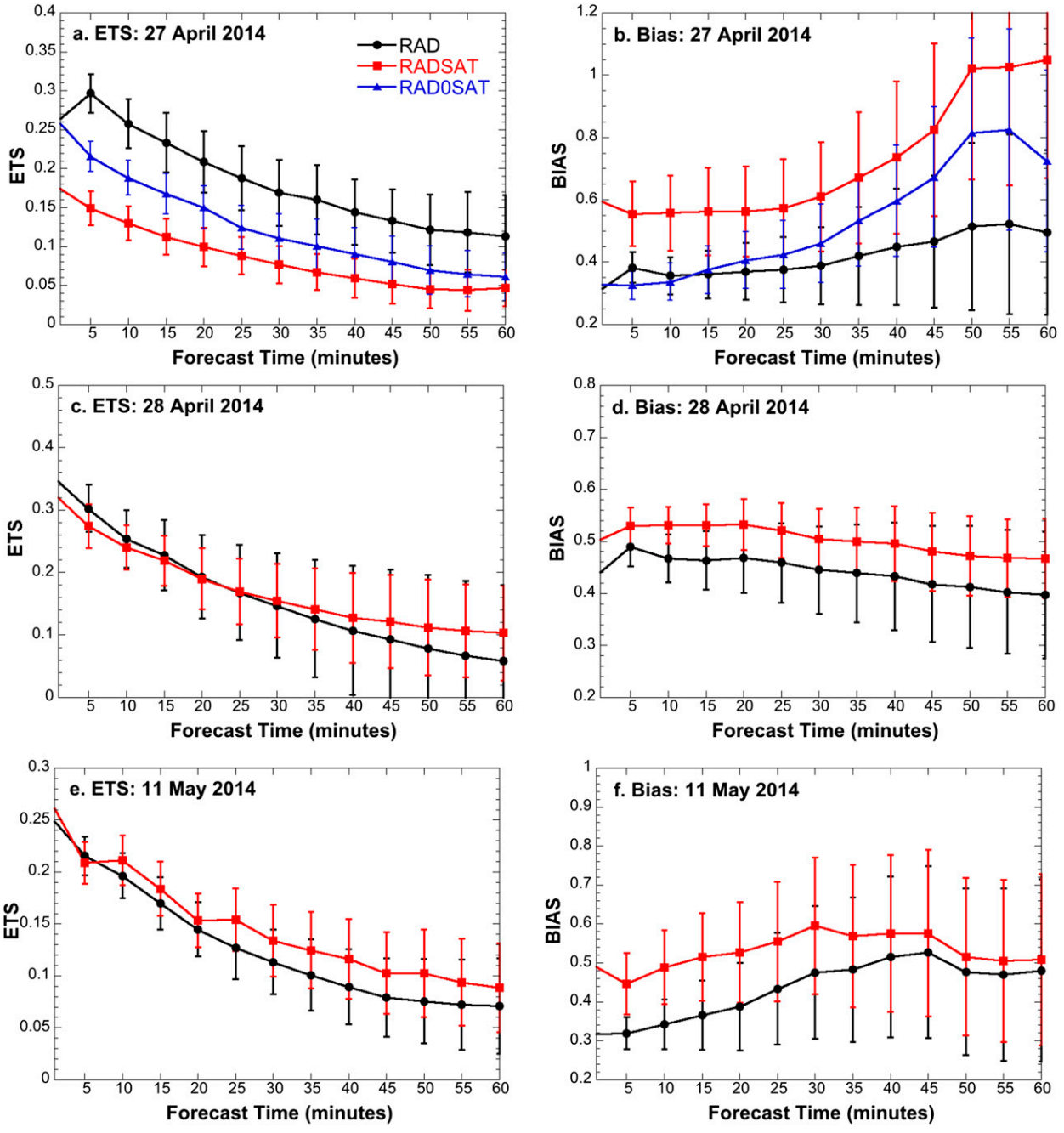

FIG. 14. As in Fig. 7, but for (a),(b) 27 Apr, (c),(d) 28 Apr, and (e),(f) 11 May 2014 events.

system that produced widespread severe weather in Iowa, which is described in detail in Part I. However, this research focuses on the early tornadic phase of development. The location of the front is evident in both experiments at 2100 UTC with ensemble mean surface temperature showing a southwest-to-northeast-oriented sharp gradient (Figs. 17a,b). RADSAT is generally warmer in the eastern portion of the domain and cooler in the southwest. The SWDOWN analyses shows why this difference is present. Both experiments generate a cloud shield associated with the tornadic storm in Nebraska with a large area of stratiform cloud cover behind the front (Figs. 17c,d). However, RAD also generates significant cloud cover east of the ongoing convection, reducing SWDOWN compared to RAD. Visible imagery at this time shows no extensive cloud coverage in this area (Fig. 17e). RADSAT also better analyzes the developing convection in northern Kansas, generating a

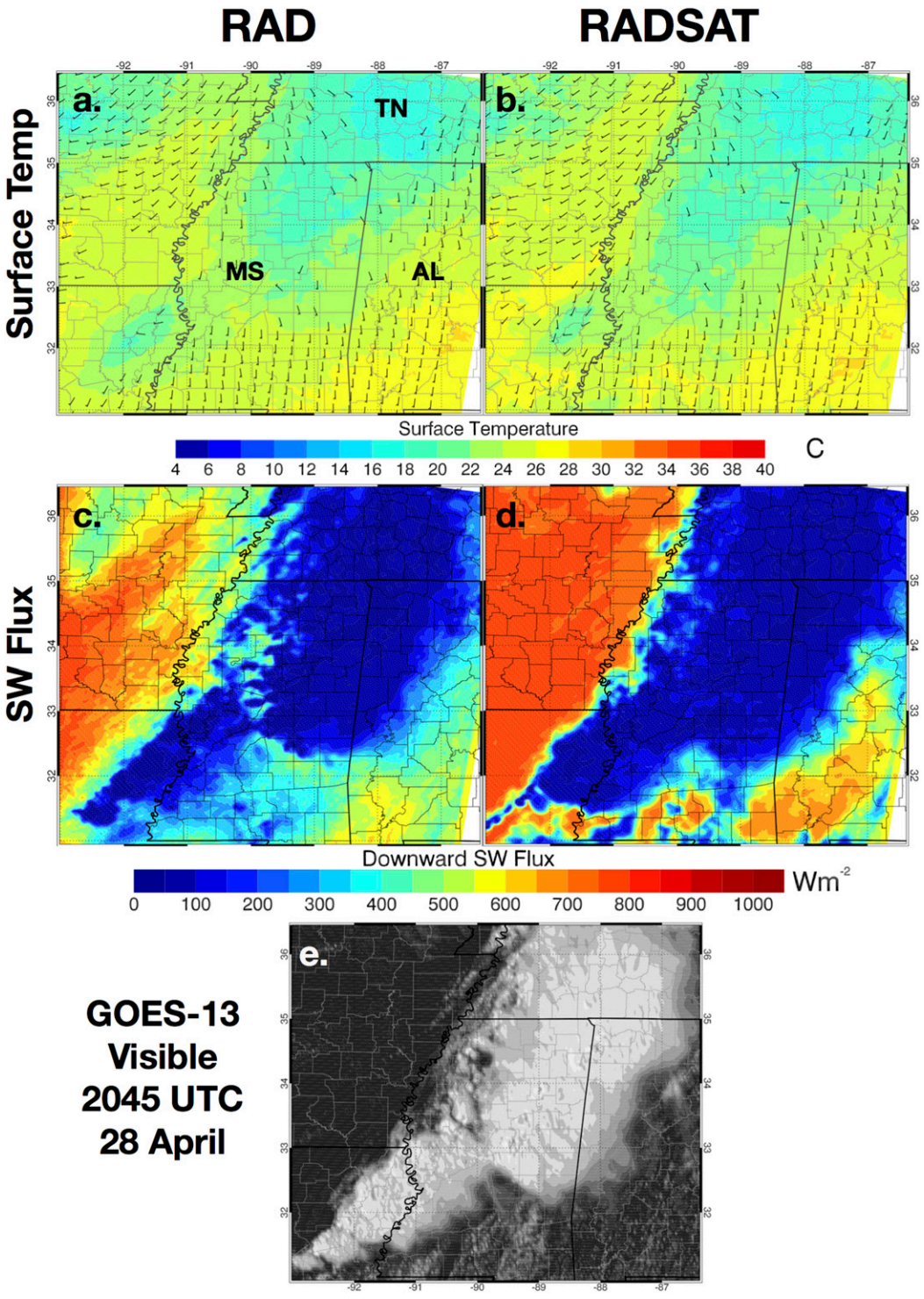

FIG. 15. As in Fig. 8, but for 2045 UTC 28 Apr 2014.

SWDOWN analysis more consistent with observations compared to RAD.

Ensemble mean 3-km reflectivity at 2100 UTC shows that both experiments analyze the tornadic storm in Nebraska well (Figs. 18a,b). As with previous events, RADSAT generates areas of light precipitation surrounding the storm core not present in RAD. However, RADSAT also correctly analyzes the storms

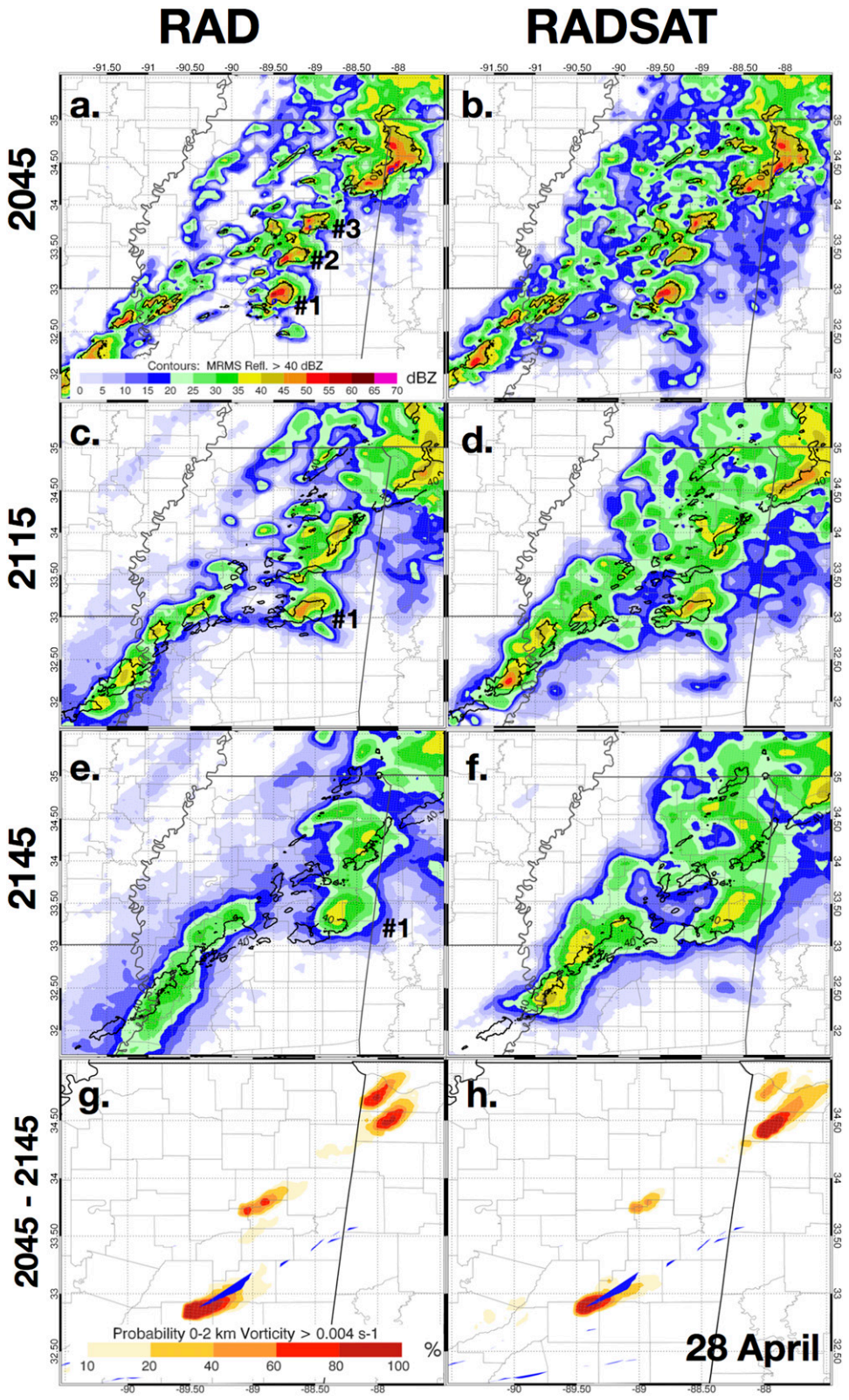

FIG. 16. As in Fig. 9, but for forecasts initiated at 2045 UTC 28 Apr 2014.

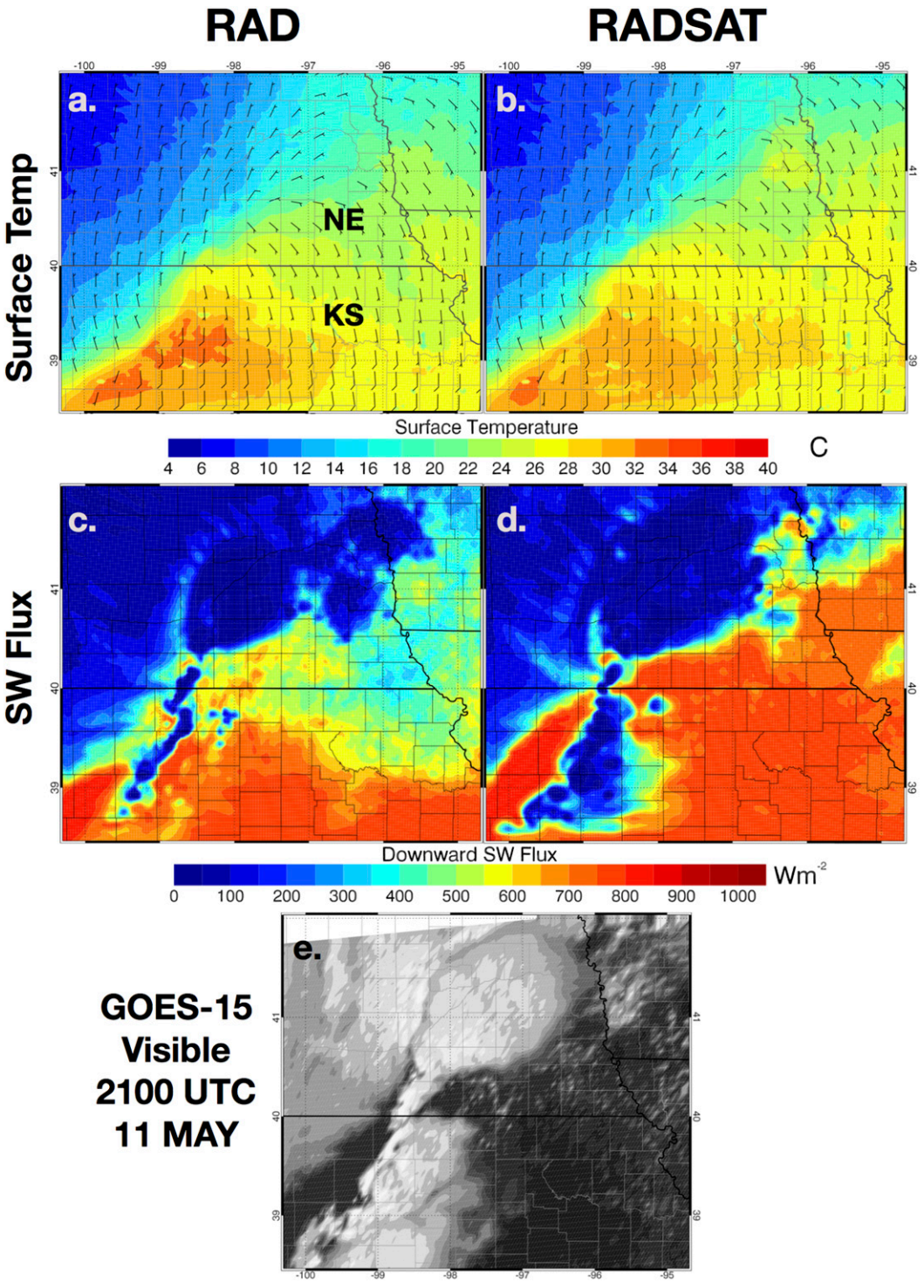

FIG. 17. As in Fig. 8, but for 2100 UTC 11 May 2014.

developing in Kansas. Similar trends are evident in the 30-min forecast at 2130 UTC with the tornadic storm still being analyzed well by both experiments while RADSAT does better with the southern storms (Figs. 18c,d). The 1-h forecast at 2200 UTC shows similar results. However, the 0–2-km vorticity probability swath paints a somewhat different picture. RAD generates probabilities greater than 80% initially that

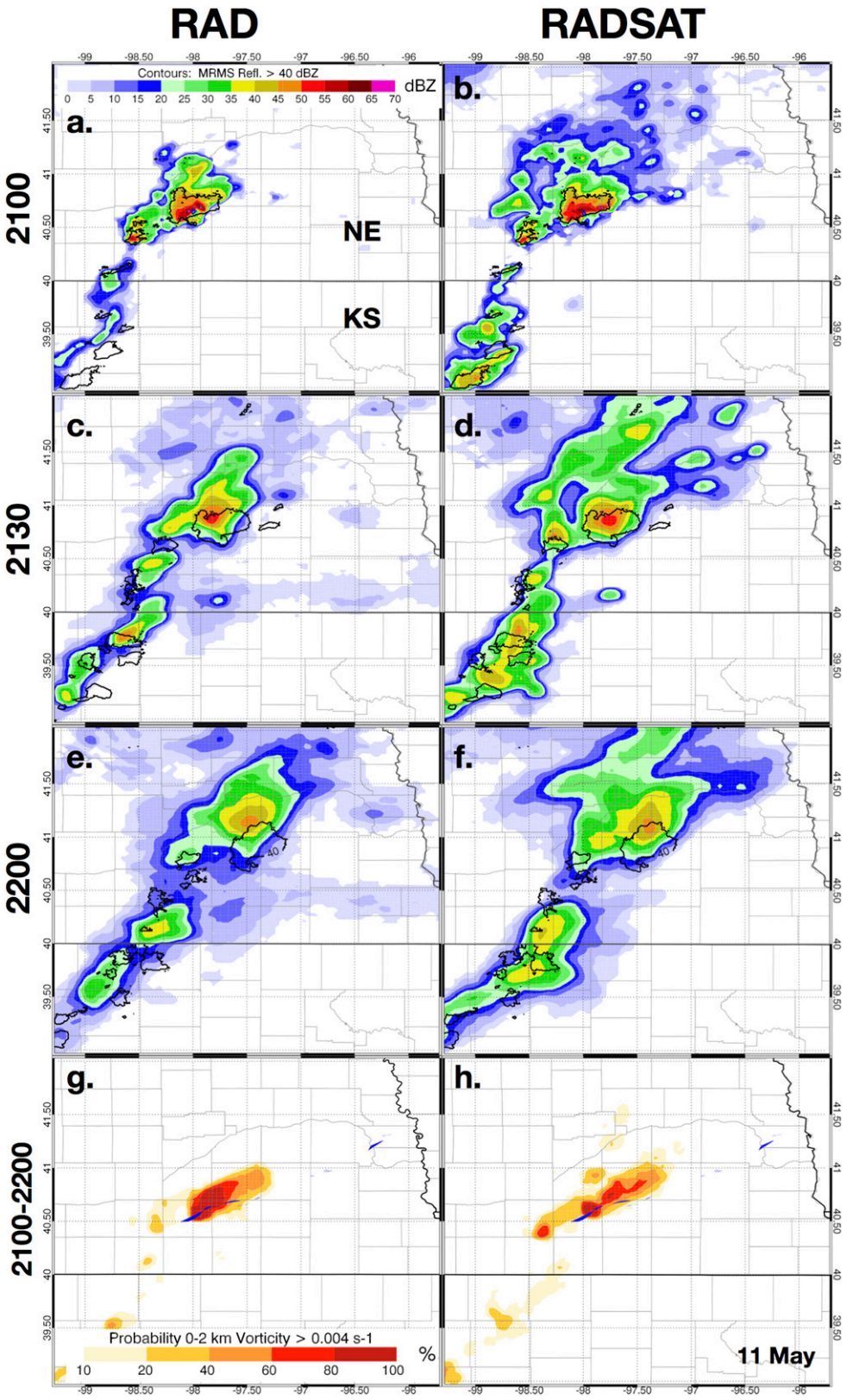

FIG. 18. As in Fig. 9, but for forecasts initiated at 2100 UTC 11 May 2014.

slowly decrease with time and are slightly north of the observed tornado track (Fig. 18g). Conversely, RADSAT generates a somewhat discontinuous swath with probabilities initially being high, before decreasing and then increasing again (Fig. 18h). ETSs for 1-h 3-km reflectivity forecasts initiated at 2030, 2045, 2100, 2115, and 2130 UTC 11 May show that RADSAT has better skill for almost all forecast times, though the skill for both decreases as a function of time, and the overall differences for this event are small (Fig. 14e). A larger difference exists in the biases, with RAD substantially underforecasting reflectivity compared to RAD during the first 30 min, after which the biases converge (Fig. 14f).

6. Conclusions

Assimilating IWP and LWP retrievals with radar reflectivity and radial velocity in the prototype WoF ensemble system provided mixed results. For the more isolated cases during 2013 and 11 May 2014, assimilating IWP and LWP improved the cloud analysis, reducing surface temperature errors in later forecasts. Replacing clear-air reflectivity with clear-sky satellite observations also yielded positive results in the clear-sky regions by reducing anomalous cloud cover present in the radar-only experiments. The improved thermodynamic conditions often generated higher-probability low-level vorticity swaths that were better placed when compared against the observed tornado track. Forecast skill for reflectivity > 40 dBZ is greater for RADSAT compared to RAD, especially over the 30-min to 1-h forecast period for these events.

However, assimilating satellite retrievals produced some unwanted artifacts. For the 27 and 28 April 2014 events, RADSAT increased cloud and light precipitation coverage compared to RAD. As a result, the storms of interest were often analyzed as too weak, leading to their rapid demise in ensuing forecasts. Assimilating clear-air reflectivity along with satellite observations into an additional experiment for 27 April reduced the spurious precipitation to a large degree while leaving the overall satellite-influenced cloud and thermodynamic features in place. Still, the resulting forecast was no better than those from the original RAD experiment. As discussed in Part I, these high-shear, lower-CAPE environments that have large areas of ongoing convection represent the most difficult cases to forecast and continued research is ongoing on how to best assimilate remote-sensing observations for these types of events. While the differences between the RAD and RADSAT experiments are intriguing and offer potential conditions in which satellite observations may improve storm-scale forecasts, the number of case studies considered in this investigation is not enough to truly indicate whether or not these differences are statistically significant.

Several important lessons were learned during the course of these experiments that will form the basis for more optimal assimilation of combined radar and satellite datasets in the future. One consistent result among all the experiments is that assimilating satellite observations while not including clear-air reflectivity resulted in areas of light precipitation where satellite observations indicated thick clouds. Over multiple assimilation cycles, these clouds eventually produce precipitation since no suppression mechanism is present. Returning clear-air reflectivity addressed this problem, but introduced another problem in the 19 May event whereby assimilating large amounts of clear-air reflectivity and cloud-free satellite observations slowed the formation of storms and/or reduced the intensity of ongoing storms. These results suggest the need for a more robust handling of combined radar and satellite datasets going forward to remove the potential for correlated observations and observation errors that cause unwanted impacts on the model analyses and ensuing forecasts. How best to determine this combination is the focus of ongoing research that hopes to improve the modest results found in this study.

Acknowledgments. This research was supported by the NOAA/National Environmental Satellite, Data, and Information Service as part of the GOES-R program. Partial funding for this research was also provided by NOAA/Office of Oceanic and Atmospheric Research under NOAA–University of Oklahoma Cooperative Agreement NA11OAR4320072, under the U.S. Department of Commerce. PM and RP are supported by the NASA Modeling, Analysis, and Prediction (MAP) program, and by the Department of Energy's Atmospheric Science Research Program under Interagency Agreement DE-SC0000991/006. The near-real-time satellite analyses can be accessed for a variety of domains online (http://cloudsgate2.larc.nasa.gov/). The computing for this project was performed at the University of Oklahoma's (OU) Supercomputing Center for Education and Research (OSCER).

REFERENCES

Aksoy, A., D. Dowell, and C. Snyder, 2009: A multicase comparative assessment of the ensemble Kalman filter for assimilation of radar observations. Part I: Storm-scale analyses. *Mon. Wea. Rev.*, **137**, 1805–1824, doi:10.1175/2008MWR2691.1.

——, ——, and ——, 2010: A multicase comparative assessment of the ensemble Kalman filter for assimilation of radar observations. Part II: Short-range ensemble forecasts. *Mon. Wea. Rev.*, **138**, 1273–1292, doi:10.1175/2009MWR3086.1.

Anderson, J. L., 2001: An ensemble adjustment filter for data assimilation. *Mon. Wea. Rev.*, **129**, 2884–2903, doi:10.1175/1520-0493(2001)129<2884:AEAKFF>2.0.CO;2.

——, 2007: An adaptive covariance inflation error correction algorithm for ensemble filters. *Tellus*, **59A**, 210–224, doi:10.1111/j.1600-0870.2006.00216.x.

——, 2009: Spatially and temporally varying adaptive covariance inflation for ensemble filters. *Tellus*, **61A**, 72–83, doi:10.1111/j.1600-0870.2008.00361.x.

——, and N. Collins, 2007: Scalable implementations of ensemble filter algorithms for data assimilation. *J. Atmos. Oceanic Technol.*, **24**, 1452–1463, doi:10.1175/JTECH2049.1.

——, T. Hoar, K. Raeder, H. Liu, N. Collins, R. Torn, and A. Avellano, 2009: The Data Assimilation Research Testbed: A community facility. *Bull. Amer. Meteor. Soc.*, **90**, 1283–1296, doi:10.1175/2009BAMS2618.1.

Chang, F.-L., P. Minnis, B. Lin, M. Khaiyer, R. Palikonda, and D. Spangenberg, 2010: A modified method for inferring cloud top height using *GOES-12* imager 10.7 and 13.3 μm data. *J. Geophys. Res.*, **115**, D06208, doi:10.1029/2009JD012304.

Crum, T. D., and R. L. Alberty, 1993: The WSR-88D and the WSR-88D Operational Support Facility. *Bull. Amer. Meteor. Soc.*, **74**, 1669–1687, doi:10.1175/1520-0477(1993)074<1669:TWATWO>2.0.CO;2.

Dawson, D. T., II, L. J. Wicker, E. R. Mansell, and R. L. Tanamachi, 2012: Impact of the environmental low-level wind profile on ensemble forecasts of the 4 May 2007 Greensburg, Kansas, tornadic storm and associated mesocyclones. *Mon. Wea. Rev.*, **140**, 696–716, doi:10.1175/MWR-D-11-00008.1.

Dowell, D. C., and L. J. Wicker, 2009: Additive noise for storm-scale ensemble forecasting and data assimilation. *J. Atmos. Oceanic Technol.*, **26**, 911–927, doi:10.1175/2008JTECHA1156.1.

——, F. Zhang, L. J. Wicker, C. Snyder, and N. A. Crook, 2004: Wind and temperature retrievals in the 17 May 1981 Arcadia, Oklahoma, supercell: Ensemble Kalman filter experiments. *Mon. Wea. Rev.*, **132**, 1982–2005, doi:10.1175/1520-0493(2004)132<1982:WATRIT>2.0.CO;2.

——, L. J. Wicker, and C. Snyder, 2011: Ensemble Kalman filter assimilation of radar observations of the 8 May 2003 Oklahoma City supercell: Influences of reflectivity observations on storm-scale analyses. *Mon. Wea. Rev.*, **139**, 272–294, doi:10.1175/2010MWR3438.1.

Fujita, T., D. J. Stensrud, and D. C. Dowell, 2007: Surface data assimilation using an ensemble Kalman filter approach with initial condition and model physics uncertainty. *Mon. Wea. Rev.*, **135**, 1846–1868, doi:10.1175/MWR3391.1.

Gao, J., and D. J. Stensrud, 2012: Assimilation of reflectivity data in a convective-scale, cycled 3DVAR framework with hydrometeor classification. *J. Atmos. Sci.*, **69**, 1054–1065, doi:10.1175/JAS-D-11-0162.1.

——, M. Xue, K. Brewster, and K. K. Droegemeier, 2004: A three-dimensional variational data assimilation method with recursive filter for single-Doppler radar. *J. Atmos. Oceanic Technol.*, **21**, 457–469, doi:10.1175/1520-0426(2004)021<0457:ATVDAM>2.0.CO;2.

Gaspari, G., and S. E. Cohn, 1999: Construction of correlation functions in two and three dimensions. *Quart. J. Roy. Meteor. Soc.*, **125**, 723–757, doi:10.1002/qj.49712555417.

Hu, M., and M. Xue, 2007: Impact of configurations of rapid intermittent assimilation of WSR-88D radar data for the 8 May 2003 Oklahoma City tornadic thunderstorm case. *Mon. Wea. Rev.*, **135**, 507–525, doi:10.1175/MWR3313.1.

Jones, T. A., and D. J. Stensrud, 2015: Assimilating cloud water path as a function of model cloud microphysics in an idealized simulation. *Mon. Wea. Rev.*, **143**, 2052–2081, doi:10.1175/MWR-D-14-00266.1.

——, J. Otkin, D. J. Stensrud, and K. Knopfmeier, 2013a: Assimilation of satellite infrared radiances and Doppler radar observations during a cool season observing system simulation experiment. *Mon. Wea. Rev.*, **141**, 3273–3299, doi:10.1175/MWR-D-12-00267.1.

——, D. J. Stensrud, P. Minnis, and R. Palikonda, 2013b: Evaluation of a forward operator to assimilate cloud water path into WRF-DART. *Mon. Wea. Rev.*, **141**, 2272–2289, doi:10.1175/MWR-D-12-00238.1.

——, J. Otkin, D. J. Stensrud, and K. Knopfmeier, 2014: Forecast evaluation of an observing system simulation experiment assimilating both radar and satellite data. *Mon. Wea. Rev.*, **142**, 107–124, doi:10.1175/MWR-D-13-00151.1.

——, D. J. Stensrud, L. Wicker, P. Minnis, and R. Palikonda, 2015: Simultaneous radar and satellite data storm-scale assimilation using an ensemble Kalman filter approach for 24 May 2011. *Mon. Wea. Rev.*, **143**, 165–194, doi:10.1175/MWR-D-14-00180.1.

Kain, J. S., and Coauthors, 2013: A feasibility study for probabilistic convection initiation forecasts based on explicit numerical guidance. *Bull. Amer. Meteor. Soc.*, **94**, 1213–1225, doi:10.1175/BAMS-D-11-00264.1.

Kalman, R. E., 1960: A new approach to linear filtering and prediction problems. *J. Basic Eng.*, **82**, 35–45, doi:10.1115/1.3662552.

Kerr, C. A., D. J. Stensrud, and X. Wang, 2015: Assimilation of cloud-top temperature and radar observations of an idealized splitting supercell using an observing system simulation experiment. *Mon. Wea. Rev.*, **143**, 1018–1034, doi:10.1175/MWR-D-14-00146.1.

Lu, H., and Q. Xu, 2009: Trade-offs between observation accuracy and resolutions in configuring phased-array radar velocity scans for ensemble-based storm-scale data assimilation. *J. Appl. Meteor. Climatol.*, **48**, 1230–1244, doi:10.1175/2008JAMC2009.1.

McPherson, R. A., and Coauthors, 2007: Statewide monitoring of the mesoscale environment: A technical update on the Oklahoma Mesonet. *J. Atmos. Oceanic Technol.*, **24**, 301–321, doi:10.1175/JTECH1976.1.

Mecikalski, J. R., P. Minnis, and R. Palikonda, 2013: Use of satellite derived cloud properties to quantify growing cumulus beneath cirrus clouds. *Atmos. Res.*, **120–121**, 192–201, doi:10.1016/j.atmosres.2012.08.017.

Meng, Z., and F. Zhang, 2008: Tests of an ensemble Kalman filter for mesoscale and regional-scale data assimilation. Part III: Comparison with 3DVAR in a real-data case study. *Mon. Wea. Rev.*, **136**, 522–540, doi:10.1175/2007MWR2106.1.

Menzel, W. P., and J. F. Purdom, 1994: Introducing GOES-I: The first of a new generation of geostationary operational environmental satellites. *Bull. Amer. Meteor. Soc.*, **75**, 757–781, doi:10.1175/1520-0477(1994)075<0757:IGITFO>2.0.CO;2.

Migliorini, S., 2012: On the equivalence between radiance and retrieval assimilation. *Mon. Wea. Rev.*, **140**, 258–265, doi:10.1175/MWR-D-10-05047.1.

Minnis, P., J. Huang, B. Lin, Y. Yi, R. F. Arduini, T.-F. Fan, J. K. Ayers, and G. G. Mace, 2007: Ice cloud properties in ice-over-water cloud systems using Tropical Rainfall Measuring Mission (TRMM) visible and infrared scanner and TRMM Microwave Imager data. *J. Geophys. Res.*, **112**, D06206, doi:10.1029/2006JD007626.

——, and Coauthors, 2008a: Cloud detection in non-polar regions for CERES using TRMM VIRS and *Terra* and *Aqua* MODIS data. *IEEE Trans. Geosci. Remote Sens.*, **46**, 3857–3884, doi:10.1109/TGRS.2008.2001351.

——, and Coauthors, 2008b: Near-real time cloud retrievals from operational and research meteorological satellites. *Remote Sensing of Clouds and the Atmosphere XIII*, R. H. Picard et al., Eds., International Society for Optical Engineering (SPIE Proceedings, Vol. 7107), doi:10.1117/12.800344.

——, and Coauthors, 2010: CERES edition 3 cloud retrievals. Preprints, *13th Conf. on Atmospheric Radiation*, Portland, OR, Amer. Meteor. Soc., 5.4. [Available online at https://ams.confex.com/ams/pdfpapers/171366.pdf.]

——, and Coauthors, 2011: CERES edition-2 cloud property retrievals using TRMM VIRS and *Terra* and *Aqua* MODIS data—Part I: Algorithms. *IEEE Trans. Geosci. Remote Sens.*, **49**, 4374–4400, doi:10.1109/TGRS.2011.2144601.

Otkin, J. A., 2010: Clear and cloudy sky infrared brightness temperature assimilation using an ensemble Kalman filter. *J. Geophys. Res.*, **115**, D19207, doi:10.1029/2009JD013759.

Pincus, R., R. J. P. Hofmann, J. L. Anderson, K. Raeder, N. Collins, and J. S. Whitaker, 2011: Can fully accounting for clouds in data assimilation improve short-term forecasts by global models? *Mon. Wea. Rev.*, **139**, 946–956, doi:10.1175/2010MWR3412.1.

Polkinghorne, R., and T. Vukicevic, 2011: Data assimilation of cloud-affected radiances in a cloud-resolving model. *Mon. Wea. Rev.*, **139**, 755–773, doi:10.1175/2010MWR3360.1.

——, ——, and F. Evans, 2010: Validation of cloud-resolving model background data for data assimilation. *Mon. Wea. Rev.*, **138**, 781–795, doi:10.1175/2009MWR3012.1.

Schmit, T. J., E. M. Prins, A. J. Schreiner, and J. J. Gurka, 2001: Introducing the GOES-M Imager. *Natl. Wea. Dig.*, **25**, 28–37.

Skamarock, W. C., and Coauthors, 2008: A description of the Advanced Research WRF version 3. NCAR Tech Note NCAR/TN–475+STR, 113 pp., doi:10.5065/D68S4MVH.

Smith, W. L., Jr., 2014: 4-D cloud properties from passive satellite data and applications to resolve the flight icing threat to aircraft. Ph.D. dissertation, University of Wisconsin–Madison, 165 pp.

Snyder, C., and F. Zhang, 2003: Assimilation of simulated Doppler radar observations with an ensemble Kalman filter. *Mon. Wea. Rev.*, **131**, 1663–1677, doi:10.1175//2555.1.

Stensrud, D. J., J.-W. Bao, and T. T. Warner, 2000: Using initial condition and model physics perturbations in short-range ensemble simulations of mesoscale convective systems. *Mon. Wea. Rev.*, **128**, 2077–2107, doi:10.1175/1520-0493(2000)128<2077:UICAMP>2.0.CO;2.

——, and Coauthors, 2009: Convective-scale Warn-on-Forecast system: A vision for 2020. *Bull. Amer. Meteor. Soc.*, **90**, 1487–1499, doi:10.1175/2009BAMS2795.1.

——, and Coauthors, 2013: Progress and challenges with Warn-on-Forecast. *Atmos. Res.*, **123**, 2–16, doi:10.1016/j.atmosres.2012.04.004.

Thompson, G., R. M. Rasmussen, and K. Manning, 2004: Explicit forecasts of winter precipitation using an improved bulk microphysics scheme. Part I: Description and sensitivity analysis. *Mon. Wea. Rev.*, **132**, 519–542, doi:10.1175/1520-0493(2004)132<0519:EFOWPU>2.0.CO;2.

——, P. R. Field, R. M. Rasmussen, and W. R. Hall, 2008: Explicit forecasts of winter precipitation using an improved bulk microphysics scheme. Part II: Implementation of a new snow parameterization. *Mon. Wea. Rev.*, **136**, 5095–5115, doi:10.1175/2008MWR2387.1.

Tong, M., and M. Xue, 2005: Ensemble Kalman filter assimilation of Doppler radar data with a compressible nonhydrostatic model: OSS experiments. *Mon. Wea. Rev.*, **133**, 1789–1807, doi:10.1175/MWR2898.1.

Vukicevic, T., T. Greenwald, M. Zupanski, D. Zupanski, T. Vonder Haar, and A. Jones, 2004: Mesoscale cloud state estimation from visible and infrared satellite radiances. *Mon. Wea. Rev.*, **132**, 3066–3077, doi:10.1175/MWR2837.1.

——, M. Sengupta, A. S. Jones, and T. Vonder Haar, 2006: Cloud-resolving satellite data assimilation: Information content of IR window observations and uncertainties in estimation. *J. Atmos. Sci.*, **63**, 901–919, doi:10.1175/JAS3639.1.

Wang, C., and X. Huang, 2014: Parallax correction in the analysis of multiple satellite data sets. *IEEE Geosci. Remote Sens. Lett.*, **11**, 965–969, doi:10.1109/LGRS.2013.2283573.

Wheatley, D. M., and D. J. Stensrud, 2010: The impact of assimilating surface pressure observations on severe weather events in a WRF mesoscale ensemble system. *Mon. Wea. Rev.*, **138**, 1673–1694, doi:10.1175/2009MWR3042.1.

——, N. Yussouf, and D. J. Stensrud, 2014: Ensemble Kalman filter analyses and forecasts of a severe mesoscale convective system using different choices of microphysics schemes. *Mon. Wea. Rev.*, **142**, 3243–3263, doi:10.1175/MWR-D-13-00260.1.

——, K. H. Knopfmeier, T. A. Jones, and G. J. Creager, 2015: Storm-scale data assimilation and ensemble forecasting with the NSSL Experimental Warn-on-Forecast System. Part I: Radar data experiments. *Wea. Forecasting*, **30**, 1795–1817, doi:10.1175/WAF-D-15-0043.1.

Wilks, D. S., 2006: *Statistical Methods in the Atmospheric Sciences.* 2nd ed. Academic Press, 627 pp.

Yussouf, N., and D. J. Stensrud, 2010: Impact of phased-array radar observations over a short assimilation period: Observing system simulation experiments using an ensemble Kalman filter. *Mon. Wea. Rev.*, **138**, 517–538, doi:10.1175/2009MWR2925.1.

——, E. R. Mansell, L. J. Wicker, D. M. Wheatley, and D. J. Stensrud, 2013: The ensemble Kalman filter analyses and forecasts of the 8 May 2003 Oklahoma City tornadic supercell storm using single- and double-moment microphysics schemes. *Mon. Wea. Rev.*, **141**, 3388–3412, doi:10.1175/MWR-D-12-00237.1.

Zhang, F., C. Snyder, and J. Sun, 2004: Impacts of initial estimate and observation availability on convective-scale data assimilation with an ensemble Kalman filter. *Mon. Wea. Rev.*, **132**, 1238–1253, doi:10.1175/1520-0493(2004)132<1238:IOIEAO>2.0.CO;2.

Zhang, S. Q., M. Zupanski, A. Y. Hou, X. Lin, and S. H. Cheung, 2013: Assimilation of precipitation-affected radiances in a cloud-resolving WRF ensemble data assimilation system. *Mon. Wea. Rev.*, **141**, 754–772, doi:10.1175/MWR-D-12-00055.1.

Zupanski, D., S. Q. Zhang, M. Zupanski, A. Y. Hou, and S. H. Cheung, 2011: A prototype WRF-based ensemble data assimilation system for dynamically downscaling satellite precipitation observations. *J. Hydrometeor.*, **12**, 118–134, doi:10.1175/2010JHM1271.1.